Special Topic

Atomic collisional data for neutral beam modeling in fusion plasmas

C. Hill[1,*] ⓘ, Dipti[1] ⓘ, K. Heinola[1] ⓘ, A. Dubois[2], N. Sisourat[2] ⓘ, A. Taoutioui[3] ⓘ,
H. Agueny[4], K. Tőkési[5] ⓘ, I. Ziaeian[5] ⓘ, C. Illescas[6] ⓘ, A. Jorge[6], L. Méndez[6] ⓘ,
A.S. Kadyrov[7] ⓘ, N.W. Antonio[7] ⓘ, A.M. Kotian[7] ⓘ, T. Kirchner[8], A.C.K. Leung[8] ⓘ,
J. Ko[9,10] ⓘ, J.K. Lee[9,10] ⓘ, O. Marchuk[11], M.G. O'Mullane[12,13] ⓘ, E. Litherland-Smith[13],
G.I. Pokol[14,15], O. Asztalos[14,15] ⓘ, P. Balazs[14,15], Y. Wu[16], C.C. Jia[16], L. Liu[16] ⓘ
and J.G. Wang[16]

[1] International Atomic Energy Agency, Vienna A-1400, Austria
[2] Sorbonne Université, CNRS, Laboratoire de Chimie Physique—Matière et Rayonnement, Paris, F-75005, France
[3] MTA Atomki Lendület Quantum Correlations Research Group, Institute for Nuclear Research, Debrecen, P.O. Box 51, H-4001, Hungary
[4] IT Division, University of Bergen, N-5020 Bergen, Norway
[5] Institute for Nuclear Research, (ATOMKI), Debrecen 4026, Hungary
[6] Departamento de Química, Facultad de Ciencias, Universidad Autónoma de Madrid, Madrid, Spain
[7] Department of Physics, Curtin University, Perth, Australia
[8] Department of Physics and Astronomy, York University, Toronto, Ontario M3J 1P3, Canada
[9] Korea Institute of Fusion Energy, Daejeon, Korea, Republic Of
[10] Department of Plasma and Nuclear Fusion, University of Science and Technology, Daejeon, Korea, Republic Of
[11] Institut für Energie- und Klimaforschung—Plasmaphysik, Partner of the Trilateral Euregio Cluster (TEC), Forschungszentrum Jülich GmbH, 52425 Jülich, Germany
[12] Department of Physics, University of Strathclyde, Glasgow, United Kingdom of Great Britain and Northern Ireland
[13] UK Atomic Energy Authority, Culham Science Centre, Abingdon OX14 3DB, United Kingdom of Great Britain and Northern Ireland
[14] Institute of Nuclear Techniques, Budapest University of Technology and Economics, Budapest, Hungary
[15] Fusion Plasma Physics Department, Centre For Energy Research, Budapest, Hungary
[16] Key Laboratory of Computational Physics, Institute of Applied Physics and Computational Mathematics (IAPCM), Beijing, China

E-mail: ch.hill@iaea.org

CrossMark

Abstract

The injection of energetic neutral particles into the plasma of magnetic confinement fusion reactors is a widely-accepted method for heating such plasmas; various types of neutral beam are also used for diagnostic purposes. Accurate atomic data are required to properly model

---

* Author to whom any correspondence should be addressed.

beam penetration into the plasma and to interpret photoemission spectra from both the beam particles themselves (e.g. beam emission spectroscopy) and from plasma impurities with which they interact (e.g. charge exchange recombination spectroscopy). This paper reviews and compares theoretical methods for calculating ionization, excitation and charge exchange cross sections applied to several important processes relevant to neutral hydrogen beams, including $H + Be^{4+}$ and $H + H^+$. In particular, a new cross section for the proton-impact ionization of H (1s) is recommended which is significantly larger than that previously accepted at fusion-relevant energies. Coefficients for an empirical fit function to this cross section and to that of the first excited states of H are provided and uncertainties estimated. The propagation of uncertainties in this cross section in modeling codes under JET-like conditions has been studied and the newly-recommended values determined to have a significant effect on the predicted beam attenuation. In addition to accurate calculations of collisional atomic data, the use of these data in codes modeling beam penetration and photoemission for fusion-relevant plasma density and temperature profiles is discussed. In particular, the discrepancies in the modeling of impurities are reported. The present paper originates from a Coordinated Research Project (CRP) on the topic of fundamental atomic data for neutral beam modeling that the International Atomic Energy Agency (IAEA) ran from 2017 to 2022; this project brought together ten research groups in the fields of fusion plasma modeling and collisional cross section calculations. Data calculated during the CRP is summarized in an appendix and is available online in the IAEA's atomic database, CollisionDB.

Keywords: neutral beams, atomic data, diagnostics, photoemission, beam penetration, collision cross sections

(Some figures may appear in colour only in the online journal)

1. Introduction and background

The most widely proposed experiments directed towards nuclear fusion energy production rely on the reaction of the hydrogen isotopes deuterium (D) and tritium (T), forming helium (He) and releasing 14 MeV neutrons. In the magnetic confinement approach to fusion D–T plasma at a temperature of around 15 keV (about 170 million K) is trapped in a toroidal magnetic field of about 3–7 T inside a vacuum vessel. Although, in principle, the high temperature of the core plasma in a fusion reactor power plant could be maintained by the fusion reaction itself, in many practical scenarios (and certainly for present and planned experimental devices such as ITER), external heating is required [1].

It is generally accepted that one of the methods best-suited to heat the confined plasma is through the injection of a beam of energetic neutral particles; this is also the approach intended to be used for power control and diagnostics in present and future devices such as ITER. The beam particles become ionized and thermalized through collisions with the plasma electrons and ions. For heating, the neutral beam (NB) particles are normally the same as the main plasma species, i.e. H or D for a hydrogen or deuterium plasma. The particle energy for neutral beam heating ranges from 10s of keV in present experiments to 1 MeV.

Neutral beam injection is also an important tool for active beam plasma spectroscopy, which may rely on the heating beam or for which a dedicated diagnostic neutral beam can be used. Some diagnostics, such as Beam Emission Spectroscopy (BES) [2] and Motional Stark Effect (MSE) measurements [3], are based on photoemission from the beam particles. On the

other hand, Charge Exchange Recombination Spectroscopy (CXRS or CHERS) [4, 5], employs emissions from plasma impurities after a charge transfer collision with a neutral beam particle. Modeling the beam penetration into the plasma and of the spectroscopic emission signals relies on detailed and accurate data for atomic processes that involve the neutral beam particles [6]. Despite the importance of the data, there are significant gaps, especially in relation to processes involving excited states of the neutral atom [7]. Moreover, the collisional processes take place in the presence of a strong electromagnetic field which puts its own restrictions on the application of the data and at the same time calls for atomic data between magnetic levels [8]. For processes involving the ground state of the neutral atom, there are often several calculated or measured data obtained using different approximations or experimental methods, and it is important to assess their uncertainties with a view to recommending the best data. Whereas both electron-atom and ion-atom collisions take place in the plasma, the primary role in active beam spectroscopy using H or D atoms is played by the latter: excitation of bound electrons through energy transfer between heavy particles. Electron collisions are in contrast more dominant for the penetration of low energy He, Li or Na beams at the edge of fusion devices [9]. Particularly important for beam modeling in fusion plasmas are the collisional data for proton–H scattering, which is also the simplest system to fundamentally understand ion-atom collisions. This process governs the beam attenuation in the plasma. Therefore, a large amount of experimental [10–16] and theoretical data [17–29] exists on this system, including the recommended data [6]. Theoretical calculations reproduce the experimental

data reasonably well for the dominant channels for the processes such as excitation and electron capture. However, there is a large discrepancy between experimental and theoretical cross sections for the ionization of H by protons at its peak, as shown in figure 1. Recommended ionization cross sections for the energy range $10\,\text{keV}\,\text{u}^{-1}$ – $1.0\,\text{MeV}\,\text{u}^{-1}$ are based on the experimental cross sections of Shah *et al* [10, 11], which also agrees with the theoretical cross sections available at that time for the low and high energy region [30–32]. However, later measurements [12] showed a significant difference in the ionization cross sections compared to earlier measurements [10, 11]. On the other hand, a detailed theoretical investigation of the two-center close-coupling method [18] also showed that the earlier theoretical results [30] did not converge and were underestimated. Other theoretical calculations [17, 20, 33] also predicted the peak ionization cross sections to be higher than the recommended values. The error, of about 20% in the ionization cross sections, can result in a factor of two difference in the beam density at center of ITER plasma for the diagnostic neutral beam (H, $100\,\text{keV}\,\text{u}^{-1}$) [34]. Therefore, it is necessary to review these newly published results with the aim of recommending the best data. The International Atomic Energy Agency (IAEA) organized a Coordinated Research Project (CRP) on the topic 'Data for Atomic Processes of Neutral Beams in Fusion Plasma'[17] that ran from 2017 to 2022 to bring together both researchers involved in the modeling of neutral beam penetration and photoemission and those involved in the calculation of collisional cross sections for excitation, ionization and charge exchange processes relevant to such modeling. This article reviews the data produced by this project and recommends cross section data sets for specific processes and computational methods for different energy regions (sections 2–4) and provides an account of benchmarking and code comparison activities for neutral beam modeling in section 5. Recommended data is available from the IAEA's online databases ALADDIN2 and CollisionDB, which are described in section 6. Atomic units (a.u.) are used throughout unless otherwise stated.

This article is divided into seven sections. After the present introduction, section 2 describes the five broad classes of computational methods compared in the calculation of ionization, excitation and charge exchange cross sections. Section 3 presents the results of this comparison applied to the $H + Be^{4+}$ collisional system (for hydrogen in both its 1s and 2s states) and discusses the reasons for and implications of the differences found. Section 4 compares new calculations of proton-hydrogen cross sections for ionization and charge exchange with previous calculations and the limited amount of experimental data available; new recommendations and analytical fits for these processes are proposed and justified for H in each of its 1s, 2s and 2p states. Section 5 reviews the use of atomic data in the modeling of penetration, photoemission and CXRS of neutral beams, reports the analysis of new CXRS data from KSTAR and, through an error propagation study, demonstrates
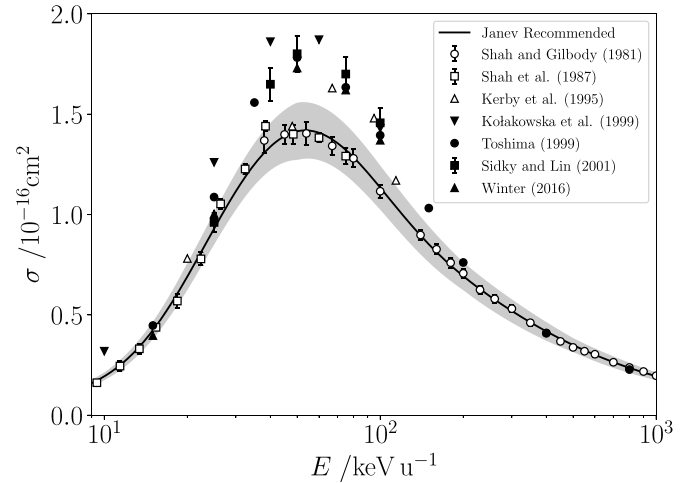
Figure 1. Experimental, calculated, and previously recommended cross sections for proton-impact ionization of ground-state hydrogen. Open circles with error bars: experiment by Shah and Gilbody [10]; open squares with error bars: experiment by Shah *et al* [11]; open up triangles with error bars: experiment by Kerby *et al* [12]; solid down triangles: theoretical cross sections obtained using the finite difference method by Kołakowska *et al* [17]; solid circles: two-center close-coupling calculations of Toshima [18]; solid squares with error bars: two-center momentum space discretization method of Sidky and Lin [33]; solid up triangles: results with Sturmian method by Winter [19]; and solid line with uncertainty interval band: recommended cross sections obtained from the fit function [6].

the importance of the new proton-impact ionization cross section to neutral beam attenuation modeling. Section 6 briefly describes the IAEA databases CollisionDB and ALADDIN, in which collisional data from this and other published studies are compiled and searchable online; finally, section 7 summarizes the conclusions of this article.

2. Description of theoretical methods

The main classes of theoretical methods used in the calculation of cross sections relevant to neutral beam modeling are described in the subsections below and are summarized in table 1.

2.1. Wave-packet convergent close-coupling method

Below we provide a brief overview of the wave-packet convergent close-coupling (WP-CCC) approach to collisions of bare ions with atomic hydrogen. The details of the WP-CCC method have been given in [35, 36]. Collisions of bare ions with atomic hydrogen is a three-body Coulomb scattering problem. It is governed by the fully quantum-mechanical three-body Schrödinger equation

$$H\Psi_i^+ = E\Psi_i^+, \tag{1}$$

where H is the full Hamiltonian of the three-body system and E is the total energy. The total scattering wave function Ψ_i^+ satisfies the outgoing-wave boundary condition. The subscript i refers to the initial channel which the wave developed from.

Table 1. A summary of the theoretical methods described in this paper and used in the calculation of cross sections relevant to neutral beam modeling.

WP-CCC	In the WP-CCC method, the total scattering wave function is expanded using a two-center basis made of wave-packet pseudostates. The exact three-body Schrödinger equation is converted into a set of coupled-channel differential equations for time-dependent expansion coefficients. In the asymptotic region, these time-dependent coefficients represent transition amplitudes for all processes including elastic scattering, excitation, ionization, and electron capture. *Advantages*: The WP-CCC method accurately solves the scattering problem by systematically increasing the size of the calculations until the results converge. The approach is particularly suited to differential ionization studies as it allows one to generate pseudostates with arbitrary energies and distributions, taking into account both direct ionization of the target and electron capture to the continuum of the projectile. *Disadvantages*: Computational complexity: WP-CCC calculations require GPU-based supercomputers.
GTDSE	A theoretical method for studying ion–atom/molecule collisions which involves the direct numerical solution of the time-dependent Schrödinger equation for the electron(s) on a discrete grid in space and time whilst the nuclei follow classical trajectories. *Advantages*: The GTDSE approach can handle a wide range of collision scenarios, including non-adiabatic processes and, in principle, account for both short- and long-range interactions; it is a valuable tool to calculate electron capture and excitation cross sections at intermediate energies. *Disadvantages*: GTDSE can be computationally demanding, particularly where very dense grids are required (for example, to represent the electron capture into highly-excited orbitals); the accuracy of its results is also sensitive to the quality of the interatomic potentials used; it is not able to yield ionization cross sections if the three inelastic processes are competitive.
AOCC	For one-active-electron collision systems, AOCC is a non-perturbative, semiclassical, spectral approach for which the time-dependent wavefunction for the active electron is expanded in terms of travelling atomic orbitals centered on the two targets and projectile. The time-dependent Schrödinger equation is then solved as a set of coupled differential equations for the probability amplitudes from which cross sections are obtained. *Advantages*: wide applicability, including for atomic and molecular collisions and, by extension, for multi-electron systems; AOCC is flexible with respect to basis set choice; can describe complex scattering channels as charge transfer, excitation and ionization, through pseudostates. It can be used for a wide range of impact energies (typically from 0.1 to 1000 keV u^{-1} or so). *Disadvantages*: Computationally demanding, particularly when large basis sets are required for convergence of the results; generally incomplete and approximative treatment of the continuum; its accuracy may be limited for high energy collisions when the channels under consideration are very unlikely, i.e. when the codes require the simultaneous evaluation of probabilities with a very large range of magnitudes.
BGM	This computational method adapts the basis set used in the solution of the time-dependent Schrödinger equation as the collisional system evolves; in doing so it is able to reduce the dimensionality of the problem whilst covering a suitable subspace of Hilbert space to yield accurate results. *Advantages*: BGM can be used to model complex quantum dynamical systems without the computational demands of huge basis sets or dense grids of spatial points on which to numerically solve the TDSE. For the Coulomb interaction, explicit expressions for a hierarchy of dynamically-adapted basis states can be derived [61]. *Disadvantages*: Determining convergence of BGM calculations can be challenging in practice; the choice and precise computation of highly-nonorthonormal pseudostates needed to describe ionization processes can be complex.
CTMC	A theoretical approach to the particle dynamics based on classical mechanics: Hamilton's equations are solved for a very large number of trajectories with the initial atomic states chosen randomly and for different impact parameters; the cross sections for different scattering processes are then determined statistically from these computed trajectories. There are variants of CTMC, notably QCTMC (section 2.5.3), which attempt to capture quantum effects through the use of carefully-chosen effective potentials. *Advantages*: CTMC methods can be computationally efficient and straightforward to implement; they can handle the many-body character of the collision systems and multiple scattering channels without prior assumptions; they can give insight into the scattering mechanism itself through the time evolution of different trajectories. *Disadvantages*: As a class of classical method, even the variants of CTMC described in section 2.5 may struggle to accurately represent quantum effects, particularly at low collision energies and for highly-correlated systems; charge exchange (electron capture) may be particularly problematic because of the role of quantum exchange effects and tunneling.

The two-center expansion of the total scattering wave function assumes a solution of the following form

$$\Psi_i^+ \approx \sum_{\alpha=1}^N F_\alpha(t,\boldsymbol{b})\psi_\alpha(\boldsymbol{r})e^{i\boldsymbol{q}_\alpha \cdot \boldsymbol{\rho}} + \sum_{\beta=1}^M G_\beta(t,\boldsymbol{b})\psi_\beta(\boldsymbol{x})e^{i\boldsymbol{q}_\beta \cdot \boldsymbol{\sigma}},$$

(2)

where ψ_α and ψ_β are the target-centered and projectile-centered pseudostates, N and M are the sizes of the target and projectile bases, F_α and G_β are the time-dependent expansion coefficients, $\boldsymbol{r}$ and $\boldsymbol{x}$ are the positions of the electron relative to the target and projectile nuclei, respectively, and $\boldsymbol{b}$ is the impact parameter. The vector $\boldsymbol{q}_\alpha$ is the momentum of the projectile relative to the target in a particular quantum state α.

Similarly, $\boldsymbol{q}_\beta$ is the momentum of the outgoing atom (formed through electron capture) relative to the target nucleus, where β denotes a particular quantum state in the rearrangement channel. The Jacobi variable $\boldsymbol{\rho}$ is the position of the projectile relative to the target's center of mass and $\boldsymbol{\sigma}$ is the position of the outgoing atom's center of mass relative to the target nucleus. The positive-energy target-centered and projectile-centered pseudostates discretize the target and projectile atom continua with a required density.

We substitute the two-center expansion (2) into the Schrödinger equation (1) and project the result on each target and projectile pseudostate. At this stage, we use a semi-classical approximation where the incoming projectile is assumed to follow a straight line trajectory. Accordingly, we set $\boldsymbol{R} = \boldsymbol{b} + \boldsymbol{v}t$, where $\boldsymbol{R}$ is the position of the projectile relative to the target nucleus and $\boldsymbol{v}$ is the velocity of the projectile. This yields a set of coupled first-order differential equations for the unknown coefficients F_α and G_β. This set of equations is solved numerically subject to the initial boundary condition that assumes the target to be in a certain initial state i.

It should be noted that despite starting from the exact Schrödinger equation and using a different ansatz for the total wave function, we arrive at the same set of equations for the expansion coefficients as that obtained in the conventional close-coupling approaches described later. The approach correctly represents both target and projectile centers and does not use the concept of the so-called electron translation factor, a remedial factor required in the conventional approaches due to inadequate representation of the rearrangement channels. See [36] for further discussion of this point. There is also a subtle difference between our expansion coefficients F_α and G_β and those used in the traditional close-coupling approaches. Since the WP-CCC method is based on the exact Schrödinger equation, our coefficients are the impact-parameter representations of the corresponding full scattering amplitudes. Accordingly, they can be directly used to calculate various singly differential cross sections [37–40] without further modifications. The method has recently been used to calculate doubly differential cross sections for ion-induced ionization [41]. Below we briefly describe how the method is used to calculate integrated cross sections.

When the aforementioned set of equations is solved and the expansion coefficients are found, the probability of transition from the initial state i to a final state f is given by the squared magnitude of the corresponding coefficient as time goes to infinity. For direct scattering (DS), f has to be one of the target states. For charge exchange (CX), f must be one of the projectile states. Thus, for the transition probabilities we have

$$P_\alpha^{\mathrm{DS}}(b) = |F_\alpha(+\infty, \boldsymbol{b}) - \delta_{\alpha i}|^2 \ \text{ and } \ P_\beta^{\mathrm{CX}}(b) = |G_\beta(+\infty, \boldsymbol{b})|^2. \tag{3}$$

The cross section for the transition is then obtained by integrating over all the impact parameters, i.e.

$$\sigma_f^{\mathrm{DS(CX)}} = 2\pi \int_0^\infty b P_f^{\mathrm{DS(CX)}}(b)\, db. \tag{4}$$

The total charge-exchange cross section can be calculated by summing the individual partial cross sections for capture into bound states on the projectile (for which the energy of the projectile state is negative):

$$\sigma^{\mathrm{CX}} = \sum_{\beta \in [\varepsilon_\beta < 0]}^{M} \sigma_\beta^{\mathrm{CX}}. \tag{5}$$

The total ionization cross section is given by the sum of the direct ionization and electron capture into continuum cross sections (in both cases, the energy of the final state is positive):

$$\sigma^{\mathrm{Ion}} = \sum_{\alpha \in [\varepsilon_\alpha > 0]}^{N} \sigma_\alpha^{\mathrm{DS}} + \sum_{\beta \in [\varepsilon_\beta > 0]}^{M} \sigma_\beta^{\mathrm{CX}}. \tag{6}$$

The size of the target and projectile bases used in close-coupling calculations determine the accuracy of the results. The bases themselves depend on parameters such as the maximum principle quantum number of the bound states included, $n_{\max}$, the maximum angular momentum quantum number, $l_{\max}$, and the number of included continuum states, N_c. Thus, it is important to establish convergence in all of the presented cross sections with respect to the basis parameters in order to ensure that the results are accurate. The WP-CCC method has been applied to a number of collision systems. Results convergent with regard to parameters $n_{\max}$, $l_{\max}$ and N_c have been published in [36–40, 42–53].

In the H(1s) + p calculations presented in section 4, the maximum orbital quantum number of included states was 6. For each orbital angular momentum, the maximum principal quantum number of bound states was 10 and the number of positive-energy wave-packet pseudostates was 20. The level of convergence in the cross sections obtained using the WP-CCC method with the aforementioned set of parameter was better than 1% at all considered energies.

Calculations involving excited states are significantly more challenging than the ground state as they require a substantially larger basis to converge. This in turn increases other parameters like the maximum impact parameter, leading to a dramatic increase in computer resources needed. For ionization and charge transfer in H($2lm$) + p collisions, the impact parameter range had to be increased significantly. The level of convergence in the cross section obtained using the WP-CCC method was better than 3% at all considered energies. For detailed convergence studies, see [43].

Details of the WP-CCC calculations of H + Be^{4+} collisions (section 3) are given in [47, 49, 51]. In particular, for the H($2lm$) + Be^{4+} system, depending on energy, the maximum orbital quantum number of included states was 9, the maximum principal quantum number of bound states was 20 and the number of positive-energy wave-packet pseudostates was 22. The level of convergence in the H($2lm$) + Be^{4+} cross sections obtained using the WP-CCC method was a few percent or better at all considered energies.

2.2. The GTDSE method

The application of the lattice method Grid Time-Dependent Schrödinger equation (GTDSE) to ion-atom collisions has been explained in previous works [54, 55]. In this section we summarize the main points of this method. As in other semi-classical treatments, the nuclei follow classical trajectories while the electronic wavefunction, $\Psi(\boldsymbol{r}, t)$, is a solution of the semi-classical equation:

$$\left[H_{el} - i \left. \frac{\partial}{\partial t} \right|_{\boldsymbol{r}} \right] \Psi = 0, \tag{7}$$

which is formally analogous to the time-dependent Schrödinger equation (TDSE). For collisions between a fully stripped ion X^{q+} and the H atom, the electronic Hamiltonian has the form:

$$H_{el}[\boldsymbol{r}, R(t)] = -\frac{1}{2}\nabla_{\boldsymbol{r}}^2 + V_H + V_X + \frac{q}{R}, \tag{8}$$

where $\boldsymbol{r}$ is the electron position vector, and V_H, V_X are the Coulomb potentials for the electron interaction with both nuclei; $\boldsymbol{R}$ is the internuclear vector.

In the GTDSE method, the TDSE is solved numerically by applying a modified version of the code of Suarez *et al* [56]. The method provides the values of the function Ψ at the points of a 3D Cartesian lattice. In particular, to treat the electron capture in ion-H collisions, the origin of the electron coordinates is on the X nucleus and the H nucleus follows a straight-line trajectory with velocity $\boldsymbol{v}$ and impact parameter b. For collisions with H(1s), Ψ is initially the product of the 1s orbital and a translation factor:

$$\Psi(\boldsymbol{r}, t) \underset{t \to -\infty}{\sim} \Psi_{1s}(\boldsymbol{r} - \boldsymbol{R}) \exp\left(i\boldsymbol{v} \cdot \boldsymbol{r} - \frac{i}{2}v^2 t \right). \tag{9}$$

In practice, the integration starts a $t = -t_1$ when the electron interaction with the ion is very small and the initial wavefunction is inside the box limits. During the collision the electron is partially transferred to the ion. In the limit $t \to \infty$, the H$^+$ nucleus is out of the box and $\|\Psi\|^2$ is the electron capture probability, while $1 - \|\Psi\|^2$ is the electron density that leaves the box, including that joined to the H nucleus (elastic and excitation processes), and the ionizing density. Moreover, the projections of Ψ on the orbitals of the ion $X^{(q-1)+}$ (Φ_{nlm}^X) yield the state-selected capture probabilities:

$$P_{nlm}^X = \lim_{t \to \infty} \left| < \Phi_{nlm}^X | \Psi > \right|^2. \tag{10}$$

The lattice representation of the electronic wave function is a vector $\boldsymbol{\Psi}$, solution of the matrix equation

$$\boldsymbol{H}\boldsymbol{\Psi} = (\boldsymbol{T} + \boldsymbol{V})\boldsymbol{\Psi} = i\dot{\boldsymbol{\Psi}}. \tag{11}$$

V is a diagonal matrix that stores the values of the potential in the grid points. The kinetic energy, **T**, is a sparse matrix, calculated by applying the finite differences method. In our calculations we have employed a stencil of 15 points. This calculation scheme reduces the memory allocation and allows efficient parallelization of the code. The propagation of the electronic wave function is carried out by means of a second order differences method.

To allow the integration near the Coulomb singularities we introduce a soft core approximation. The potentials are:

$$V_H(r_H) = -\frac{1}{(r_H^2 + \epsilon_H)^{1/2}}, \quad V_X(r_X) = -\frac{q}{(r_X^2 + \epsilon_X)^{1/2}}. \tag{12}$$

The soft-core parameters $\epsilon_{H, X}$ are very small compared to the distance between neighboring grid points, and they are optimized by fitting the atomic energies for each grid density. In order to avoid unphysical reflections at the walls of the box, we have introduced a mask function (see [54]).

The GTDSE method also provides state-selected excitation probabilities. To this end, we have employed an alternative reference system with the H nucleus on the origin of the reference system. Initially we have

$$\Psi(\boldsymbol{r}, t) \underset{t \to -\infty}{\sim} \Psi_{1s}(\boldsymbol{r}) \tag{13}$$

During the collision the ion crosses the box and part of the electron density $(1 - \|\Psi\|^2)$ is lost due to capture and ionization. After the collision one can obtain the excitation probabilities as:

$$P_{nlm}^H = \lim_{t \to \infty} \left| < \Phi_{nlm}^H | \Psi > \right|^2. \tag{14}$$

The treatment of collisions with H($n = 2$) must take into account the Stark mixture of the ϕ_{2s} and $\widetilde{\phi_{2p}}$ orbitals, where $\widetilde{\phi_{2p}}$ is an orbital in the direction of the internuclear vector $\boldsymbol{R}$. In the calculations we have used a two-state perturbative approach to construct the asymptotic linear combination of these orbitals. In a second step, we have integrated numerically the TDSE with the H nucleus inside the box subject to the interaction with a distant X^{q+} ion, which is out of the box limits. Finally, the numerical wave function is used as the initial wave function for the numerical calculation with both nuclei inside the box, as in the case of collisions with H(1s).

From a practical point of view, the accuracy of the calculation is determined by the extension and the density of the grid; for instance, the calculation of capture probabilities into very excited orbitals requires the use of very large boxes to numerically describe the corresponding orbitals. Also, the grid size must permit that the initial wave function (9) is inside the box ($\|\Psi(\boldsymbol{r}, -t_1)\|^2 = 1$). The accuracy of the finite differences calculation depends on the grid density, but, obviously, the memory requirements rapidly increase with the number of grid points. The calculations of excitation and electron capture in collisions of Be^{4+} + H(1s, 2s) described in section 3 used cubic boxes with side lengths of 160 a.u. for H(2s) and 80 a.u. for H(1s), although we have taken advantage of the symmetry of the problem upon reflection in the collision plane that allows

us to consider only the grid points above this plane. The typical grid included the points $q = q_0 + \Delta_q$ with $q = x, y, z$ and $\Delta_q = 0.2$ a.u.

2.3. Atomic orbital close-coupling

The Atomic Orbital Close-Coupling (AOCC) method is a semi-classical two-center atomic orbital close-coupling method [57–59] this is suitable for the treatment of ion-atom collisions in a wide range of impact energies, say from 0.1 to 1000 keV u^{-1}. In the present AOCC implementation, the straight-line constant velocity approximation is adopted for the relative motion of the collision partners so that, as in WP-CCC and GTDSE methods described above, the internuclear vector is $\boldsymbol{R}(t) = \boldsymbol{b} + \boldsymbol{v}t$, where b is the impact parameter and v is the collision velocity. For a one-electron collision system, the time-dependent wave function of the active electron in the field of two ion cores can be expanded in terms of traveling atomic orbitals centered at the target and projectile,

$$\Psi(\boldsymbol{r}, t) = \sum_i^{N_A} a_i(t) \phi_i^A(\boldsymbol{r}) \, e^{-i\epsilon_i^A t}$$
$$+ \sum_j^{N_B} b_j(t) \phi_j^B(\boldsymbol{r} - \boldsymbol{R}(t)) \, e^{-i\epsilon_j^B t} \, e^{i\boldsymbol{v} \cdot \boldsymbol{r} - iv^2 t/2} \quad (15)$$

where the last exponential corresponds to the electron translation factor which takes into account the relative motion of the projectile orbitals with respect to the target. Here the atomic state wave function $\phi^{A,B}$ can be obtained by the diagonalization of single (target or projectile) Hamiltonian over even-tempered basis of Gaussian-type Orbitals (GTOs) [60] or Slater-type orbital (STOs), χ [26]

$$\phi(\boldsymbol{r}) = \sum_k c_k \chi_{klm}(\boldsymbol{r}) \quad (16)$$

optimized to build a set of bound states as well as pseudostates of positive and negative energy, ϵ. Note that both GTO and STO basis sets are adopted in the present AOCC work, hereinafter the corresponding calculations are referred to as AOCC-1 and AOCC-2 respectively, for the convenience of discussion. Inserting equation (15) into the time-dependent Schrödinger equation (equation (7)), one obtains a set of coupled first-order differential equations for the expansion coefficients $a_i(t)$ and $b_j(b)$

$$\dot{\boldsymbol{C}} = -i \, \boldsymbol{S}^{-1} \boldsymbol{M} \, \boldsymbol{C} \quad (17)$$

where $\boldsymbol{C}$ represents the vector of the expansion coefficents $a_i(t)$ ($i = 1, 2, \ldots, N_A$) and $b_j(t)$ ($j = i + 1, 2, \ldots, N_A + N_B$), $\boldsymbol{S}$ is the overlap matrix and $\boldsymbol{M}$ the coupling matrix. Note that equation (17) is equivalent in shape to the equations solved in WP-CCC approach (section 2.1), except that the core-core repulsion term is omitted here since it contributes only a trivial phase factor which can be accounted for in evaluation of differential cross sections. Solving the coupled channel equations under the initial conditions (for given v, b and initial state

ϕ_1^A: $a_i(t \to -\infty) = \delta_{i1}, b_j(t \to -\infty) = 0$), one can obtain the probabilities of electron capture, excitation and ionization processes. By integrating these probabilities over the impact parameter, b, the cross sections corresponding to a transition $\phi_1^A \to \phi_{i \neq 1}^A$ or ϕ_j^B can be obtained as

$$\sigma_i = 2\pi \int_0^{+\infty} |a_i(t \to +\infty)|^2 b \, db \quad (18)$$

$$\sigma_j = 2\pi \int_0^{+\infty} |b_j(t \to +\infty)|^2 b \, db. \quad (19)$$

The sum of the state-selective σ_i and σ_j give the cross sections for total electron capture, total excitation and total ionization (for i, j corresponding to continuum pseudostates).

In the present AOCC-1 calculations for $Be^{4+} - H$ collisions (section 3), the basis sets include on each center 207 GTOs with $\ell \leqslant 4$, that is 24 s, 54 p, 60 d, 42 f and 27 g orbitals. These sets of GTOs allow the description, with high precision, of the states up to $n \leqslant 5$, 34 pseudostates of negative energy, and 75 (34) pseudostates of positive energy up to 3 a.u. for the target (projectile). For the $H^+ - H$ collision system, the AOCC-1 basis sets have been described in [26]: for both collision partners, all bound states up to $n = 5$ are included, together with 136 pseudo states of energy up to 2 a.u. Note that most of the AOCC-1 results are presented in the following with confidence bars, evaluated by comparing the results from different basis sets. For $H^+ - H$ collisions, see [26]; for $Be^{4+} - H$ collisions, the confidence bars are evaluated by comparing the results obtained by three smaller basis sets, i.e. including a smaller number of GTOs for each angular momentum and/or excluding the f and g orbitals. They are certainly overestimated and provide a conservative information about the convergence of the results presented hereafter.

In the present AOCC-2 calculations for $Be^{4+} - H$ collisions, larger basis sets are used to obtain convergent results. In the electron capture cross section calculations, the basis set centered on the Be^{3+} ion includes 192 bound states ($n \leqslant 10, l \leqslant 7$) and 144 quasi-continuum pseudostates ($n = 11-14, l \leqslant 7$), and the target includes 35 bound states ($n \leqslant 5, l \leqslant 4$). In the excitation and ionization cross section calculations, the target basis includes 56 bound states ($n \leqslant 6, l \leqslant 5$) and 147 quasi-continuum pseudostates ($n = 7-13, l \leqslant 5$), while that centered on the projectile contained only the bound states with 35, $n \leqslant 5$ ($l \leqslant 4$). In the AOCC-2 calculations of $H^+ - H$ collisions, the basis sets centered on the target includes 56 bound states ($n \leqslant 6, l \leqslant 5$), while the projectile includes 65 bound states ($n \leqslant 7, l \leqslant 4$) and 90 quasi-continuum pseudostates ($n = 8-13, l \leqslant 4$). For excitation and ionization cross section calculations, the target includes 95 bound states ($n \leqslant 9, l \leqslant 4$) and 75 quasi-continuum pseudostates ($n = 10-14, l \leqslant 4$), while the basis centered on the projectile contained only bound states with 35, $n \leqslant 5$ ($l \leqslant 4$). The convergence of the electron capture, excitation and ionization cross sections has been checked with different expansion basis sets on the target and projectile at different incident energies.

2.4. Two-center basis generator method

The basis generator method (BGM) was introduced more than twenty years ago as a general approach to the solution of time-dependent quantum problems in a dynamically adapted finite subspace of Hilbert space [61]. The central idea is that if the finite model space follows the dynamics of the system reasonably well, its dimensionality does not need to be high, i.e. the number of basis states required to span it and achieve in it a reasonably well converged solution of the evolution problem may remain modest.

Two variants of the BGM have been implemented for the description of collision problems in the semi-classical approximation: a one-center based and a two-center (TC) version. For the latter, labeled TC-BGM [62], a proven track record of yielding accurate total cross sections for electron capture, excitation, and ionization in a variety of ion-atom and ion-molecule collision problems has been established over the years (see, e.g. [63–65] and references therein).

From a practical perspective, for an effective one-electron system the TC-BGM is similar to the two-center AOCC method in that a part of the basis used to represent the time-dependent wave function (15) consists of traveling bound orbitals on collision centers A and B, representing target and projectile, respectively. It differs in the way that pseudostates are constructed, which are included in addition to the atomic orbitals for the description of quasimolecular couplings at low collision energy and couplings to the continuum. In the TC-BGM, they are obtained by operating with powers of a (regularized) potential operator onto the atomic orbitals of one or both centers, thereby ingraining in them dynamical information about the two-center collision problem.

Adapting the notation of section 2.3, these pseudostates are written as

$$\chi_{i,K}^{A,B}(\boldsymbol{r},t) = [W_p(r_p)]^K \tilde{\phi}_i^{A,B}(\boldsymbol{r},t), \tag{20}$$

$$W_p(r_p) = \frac{1}{r_p}\left(1 - \mathrm{e}^{-r_p}\right), \tag{21}$$

where $r_p = |\boldsymbol{r} - \boldsymbol{R}(t)|$ is the distance between the projectile and the electron, and $\tilde{\phi}_i^{A,B}$ are atomic orbitals which include time-dependent phase factors and, depending on the reference frame chosen, the appropriate electron translation factors. For the calculations reported in this work only pseudostates obtained from operating with W_p on target orbitals (i.e. orbitals $\tilde{\phi}_i^A$) are included.

The pseudostates (20) are not normalized and are (highly) non-orthogonal among themselves and to the sets of bound target (A) and projectile (B) states. As explained in [63], a two-step orthogonalization procedure is applied in each time step of the numerical propagation to deal with this issue. At the final time, the squared moduli of the amplitudes corresponding to the bound states on both centers are interpreted as transition probabilities, and cross sections for state-selective excitation and capture are calculated as integrals over the impact parameter (cf equations (18) and (19)). The total ionization cross section is obtained by integrating the probability $p_{\mathrm{ion}} =$ $1 - p_A - p_B$, where p_A and p_B are the sums of the probabilities for an electron to be found in one of the included target or projectile states, respectively.

Convergence with respect to basis size is monitored in the usual way by comparing results obtained from different expansion sets. This can be challenging in practice since three basis subsets can be increased or decreased independently: the set of bound target states, the set of bound projectile states, and the set of BGM pseudostates. There also is a trade-off: A very large number of bound states effectively imposes a limit on the number of pseudostates that can be included in addition, since their non-orthogonality can turn into numerical linear-dependencies associated with a singular overlap matrix. For the proton-hydrogen calculations reported in [25] all bound states on both centers up to $n = 6$ plus up to about 200 pseudostates were included. For the Be^{4+} case discussed in section 3 the projectile basis set was increased up to $n = 10$ to obtain reasonably well converged results for electron capture. On the target side, the basis was restricted to the states of the first five shells and only about 50 pseudostates were added. This does not mean that the description of ionization is necessarily insufficient, but without comparison to independently obtained data the quality of the results would be difficult to assess.

2.5. Classical trajectory Monte-Carlo models

The classical trajectory Monte Carlo (CTMC) method is a well-known method to describe atomic collision and to calculate cross sections. It is particularly well suited to an unambiguous discrimination between the three inelastic processes which are strongly competing in the intermediate energy range. The CTMC model, as a classical approach, uses the planetary motion of electron under a central force. The CTMC method is a nonperturbative method, where classical equations of motions are solved numerically [66–73]. It is based on the calculation of a large number of individual particle trajectories where the initial atomic states are chosen randomly. One of the advantages of the CTMC method is that the many-body interactions are taken into account during the collisions on a classical level. In the present work, the CTMC calculations were made under five approximations. The differences between the models and how the target initial conditions are handled are presented in the following subsections.

2.5.1. Standard classical trajectory Monte-Carlo (S-CTMC) model.
In the standard three-body CTMC model the three particles (target nucleus, target electron, and projectile) are characterized by their masses and charges [69, 74, 75]. For the description of the interaction among the particles, a Coulomb potential is used. The Hamiltonian for the three particles can be written as:

$$H_0 = K + V_{\mathrm{coul}} \tag{22}$$

where K is the total kinetic energy and V_{coul} is the potential energy of the interaction system. The equations of motion are derived from the Hamilton equation and they are integrated

with respect to the time as an independent variable by the standard Runge–Kutta method for a given set of initial conditions. The origin of our coordinate system in the laboratory frame is the center-of-mass of the target atom, and the z-axis is parallel to the velocity vector of the projectile.

In the classical approaches, the classical principal quantum number (n_c) is defined by

$$n_c = Z_T Z_e \left(\frac{\mu_{Te}}{2U}\right)^{1/2}, \tag{23}$$

where μ_{Te} and U are the reduced mass of the target nucleus and the target electron, and the electron binding energy, respectively. The classical values of n_c are quantized to a specific level n if they satisfy the following relation [76]:

$$\left[(n-1)\left(n-\frac{1}{2}\right)n\right]^{1/3} < n_c \leqslant \left[n\left(n+\frac{1}{2}\right)(n+1)\right]^{1/3}. \tag{24}$$

The classical orbital angular momentum is defined by

$$\ell_c = \sqrt{(\ell_c^x)^2 + (\ell_c^y)^2 + (\ell_c^z)^2} \tag{25}$$

with,

$$\ell_c^x = m_e(y\dot{z} - \dot{y}z), \quad \ell_c^y = m_e(z\dot{x} - \dot{z}x), \quad \ell_c^z = m_e(x\dot{y} - \dot{x}y), \tag{26}$$

where x, y, and z are the Cartesian coordinates of the electron relative to the nucleus and $\dot{x}$, $\dot{y}$, and $\dot{z}$ are the corresponding velocities. Since ℓ_c is uniformly distributed for a given n level, the quantal statistical weights are reproduced by choosing bin sizes such that [76] :

$$\ell < \frac{n}{n_c}\ell_c \leqslant \ell + 1. \tag{27}$$

The total cross sections can be calculated by:

$$\sigma^{(f)} = \frac{2\pi\, b_{\max}}{T_N} \sum_j b_j^{(f)}. \tag{28}$$

The statistical uncertainty of the cross sections is given by:

$$\Delta\sigma^{(f)} = \sigma^{(f)} \left(\frac{T_N - T_N^{(f)}}{T_N T_N^{(f)}}\right)^{1/2}. \tag{29}$$

In equations (28) and (29) T_N is the total number of trajectories calculated for impact parameters less than $b_{\max}$, $T_N^{(f)}$ is the number of trajectories that satisfy the criteria for the corresponding final channels (excitation, ionization, electron capture), and $b_j^{(f)}$ is the actual impact parameter for the trajectory corresponding to the given final channel.

2.5.2. Eikonal classical trajectory Monte Carlo method. As in the semiclassical calculations of sections 2.1–2.4, this approach for bare ion impact is based on the impact parameter approximation [57], in which $\boldsymbol{R}$, the internuclear position vector, follows linear trajectories $\boldsymbol{R} = \boldsymbol{v}t + \boldsymbol{b}$, with relative nuclear velocity $\boldsymbol{v}$ and impact parameter $\boldsymbol{b}$. The electron dynamics are classically described by means of a phase space distribution $\rho(\boldsymbol{r},\boldsymbol{p},t)$, discretized in terms of $N = 2 \times 10^6$ non-interacting trajectories:

$$\rho(\boldsymbol{r},\boldsymbol{p},t) = \frac{1}{N}\sum_{j=1}^{N}\delta(\boldsymbol{r} - \boldsymbol{r}_j(t))\delta(\boldsymbol{p} - \boldsymbol{p}_j(t)) \tag{30}$$

which must satisfy the Liouville equation. The trajectories $\{\boldsymbol{r}_j(t),\boldsymbol{p}_j(t)\}$ of the distribution (30) are solutions of the Hamilton equations for the electron motion in the two-center Coulomb potential, which monitor the temporal evolution of the jth trajectory from an initial time $t_{\text{ini}} = -500/v$ a.u. up to $t_{\text{fin}} = 1000/v$ a.u. We have checked the convergence of the total and partial cross sections with respect to the statistics and the integration time. In particular, the long collision time ensures that the calculation correctly takes into account the Stark mixing in the case of collisions with H($n=2$) targets. At $t = t_{\text{fin}}$, we ascribe an electron to the capture, excitation or ionization channel depending on its energies with respect to both moving nuclei. In practice, taking the origin of the electron coordinates on the target nucleus, a captured electron presents a negative energy with respect to the projectile $\varepsilon_j^P(t_{\text{fin}}) = (\boldsymbol{p} - \boldsymbol{v})^2/2 - Z_P/|\boldsymbol{r} - \boldsymbol{b} - \boldsymbol{v}t_{\text{fin}}|$, while its energy with respect to the target, $\varepsilon_j^T(t_{\text{fin}}) = \boldsymbol{p}^2/2 - Z_T/r$, is positive. In the excitation channel, $\varepsilon_j^P(t_{\text{fin}}) > 0$ and $\varepsilon_j^T(t_{\text{fin}}) < 0$, while for ionization $\varepsilon_j^P(t_{\text{fin}}) > 0$ and $\varepsilon_j^T(t_{\text{fin}}) > 0$. Within the capture and excitation channels we can further define (n,l) levels by employing the Becker and McKellar criterion of adjacent and non-overlapping boxes [76], based on the classical-quantum correspondence principle in the $n \to \infty$ limit. For excitation, we define the classical counterparts n_c, ℓ_c to the quantum numbers n, l through:

$$n_c = \frac{Z_T}{\sqrt{-2\varepsilon^T}}, \quad \ell_c = |\boldsymbol{r} \times \boldsymbol{p}| \tag{31}$$

An excited electron is considered to belong to the (n,l) sublevel if n_c and ℓ_c fulfill equations (24) and (27). Counting the number of electrons $N_{n,l}$ fulfilling these criteria yields the state-selective probabilities $P_{n,l}(v,b) = \frac{N_{n,l}}{N}$ and the corresponding cross sections are obtained by integrating the transition probabilities over the impact parameter,

$$\sigma_{n,l} = 2\pi \int_{b_{\min}}^{b_{\max}} db\, b\, P_{n,l}(b,v) \tag{32}$$

The accuracy of the CTMC method generally depends on that of the initial distribution. This method is commonly applied using the so-called microcanonical distribution [66] (M-CTMC), in which all the electron trajectories have the

energy ϵ; that of the initial state of the target atom and has the form:

$$\rho^m(\boldsymbol{r},\boldsymbol{p};\epsilon) = \frac{(-2\epsilon)^{5/2}}{8\pi^3 Z^3}\, \delta\left(\frac{p^2}{2} - \frac{Z}{r} - \epsilon\right). \qquad (33)$$

As is well-known, the description of the H(1s) orbital using (33) implies a cut-off to the spatial distribution at $r_0 = 2$ a.u. and similarly, at $r_0 = 8$ a.u. in the case of the H($n = 2$) spatial distribution.

We have also employed a hydrogenic initial distribution [77, 78] (H-CTMC) which is constructed as a linear combination with constant coefficients of several microcanonical distributions with different energies, ϵ_k:

$$\rho^h(\boldsymbol{r},\boldsymbol{p}) = \sum_k a_k \rho_k^m(\boldsymbol{r},\boldsymbol{p}). \qquad (34)$$

The coefficients of the combination a_k are obtained by imposing that the average energy is equal to that of the corresponding quantum level, ϵ [55, 77–79]. In practice, the use of the hydrogenic distribution improves the results with respect to those of the microcanonical calculation for electron capture and ionization processes, and n-partial electron capture cross sections for relatively large n in ion-H(2s) collisions (see [54, 80]). Previous calculations [79, 81] show that the improvement is less important for collisions with H($n = 2, 3$) than for collisions with H in the ground state. In the present work, we have carried out the calculations for collisions with H(2s) by including in the initial distribution only the trajectories with l_c fulfilling (24) and (27) with $\ell = 0$.

2.5.3. Quasi-classical trajectory Monte Carlo (QCTMC) model. In 1980s, the quasi-classical trajectory Monte Carlo (QCTMC) method was proposed by Kirschbaum and Wilets [82] as an improved version of the standard CTMC model. The effective potentials were added to the usual H_0 Hamiltonian to mimic the Heisenberg uncertainty principle and the Pauli Exclusion Principle for multi-electronic systems [83]. The effectiveness of the QCTMC is elaborated in several studies [84, 85]. Despite the fact that our calculation system is the simplest system, we use the constrained potential in the description of the hydrogen atom. It was shown that significant improvement can also be reached in the one electron collision systems if the effective potential is introduced to mimic the Heisenberg uncertainty principle. In our case the Hamiltonian can be written as:

$$H_{\text{QCTMC}} = H_0 + V_H, \qquad (35)$$

where H_0 is the usual Hamiltonian containing the total kinetic energy and Coulomb potential energy terms of all bodies. The correction term is defined as:

$$V_H(\boldsymbol{r}_{\lambda e},\boldsymbol{P}_{\lambda e};\xi_H,\alpha_H)$$
$$= \frac{\xi_H^2}{4\alpha_H r_{\lambda e}^2 \mu_{\lambda e}} \exp\left\{\alpha_H\left[1 - \left(\frac{\boldsymbol{r}_{\lambda e}\cdot\boldsymbol{P}_{\lambda e}}{\xi_H}\right)^4\right]\right\}, \qquad (36)$$

where λ and e mark the nucleus (target or projectile) and the target electron, respectively. $\boldsymbol{r}_{\lambda e}$ is the relative displacement vector from the nucleus (target or projectile) to the electron and $\boldsymbol{P}_{\lambda e}$ is the corresponding relative momenta. $\mu_{\lambda e}$ is the reduced mass of the particles λ and e. The α_H and ξ_H are the Heisenberg adjustable hardness and dimensionless parameters, respectively.

The QCTMC model can, until recently, only be used for a ground state initial configuration [29, 84–92]. The α and ξ parameters of the correction term are obtained from the definition of the lowest energy according to: $\frac{\partial H}{\partial p} = 0, \frac{\partial H}{\partial r} = 0$.

In our work we applied two versions of the QCTMC model; 1) the target-centered scheme (T-QCTMC) when the correction term is taken into account between the target electron and target nucleus, and 2) the target-projectile centered scheme (C-QCTMC) when the correction term is taken into account between the target electron and both of target nucleus and projectile.

3. H + Be^{4+}: comparison of computational methods for excitation, ionization and charge exchange

In the collision energy range relevant for fusion plasma (keV u^{-1}), the so-called intermediate energy range, inelastic processes (i.e. charge exchange, excitation and ionization) are of comparable importance and are moreover strongly coupled. Non-perturbative approaches are therefore unavoidable. Several such methods have been proposed in the past and have been employed in this work (see section 2).

Despite the extensive work that has been done to describe the electron dynamics during ion-atom collisions, computing accurate cross sections for inelastic processes remains a challenging task. It is fair to state that there is currently no available method that provides accurate cross sections for all systems and/or processes. It is therefore essential to combine and compare results from different calculations.

In this work, we have employed several theoretical approaches to compute the cross sections for the different systems and collisional processes relevant for the modeling of fusion plasma. Before reporting these cross sections (see section 4), we compare the different theoretical methods for the collisional system H(1s or 2s) + Be^{4+}. The purpose of this comparison exercise is to establish the applicability of different methods to the central processes for neutral beam modeling at relevant energies. The comparison of up to 10 computational methods has been facilitated by the choice of a fixed set of processes (excitation, ionization and charge exchange) and energies (20, 100 and 500 keV u^{-1}).

The total charge exchange cross sections calculated with the different theoretical approaches for the collisional system H(1s) + Be^{4+} are shown in the upper panels of figure 2. Except at the highest collision energy, for which charge exchange is weak, the cross sections obtained with semiclassical approaches (WP-CCC, GTDSE, AOCC, TC-BGM) for this process agree with each other. At the highest energy, TC-BGM appears to overestimate the cross section for this process because of numerical instabilities related to the highly
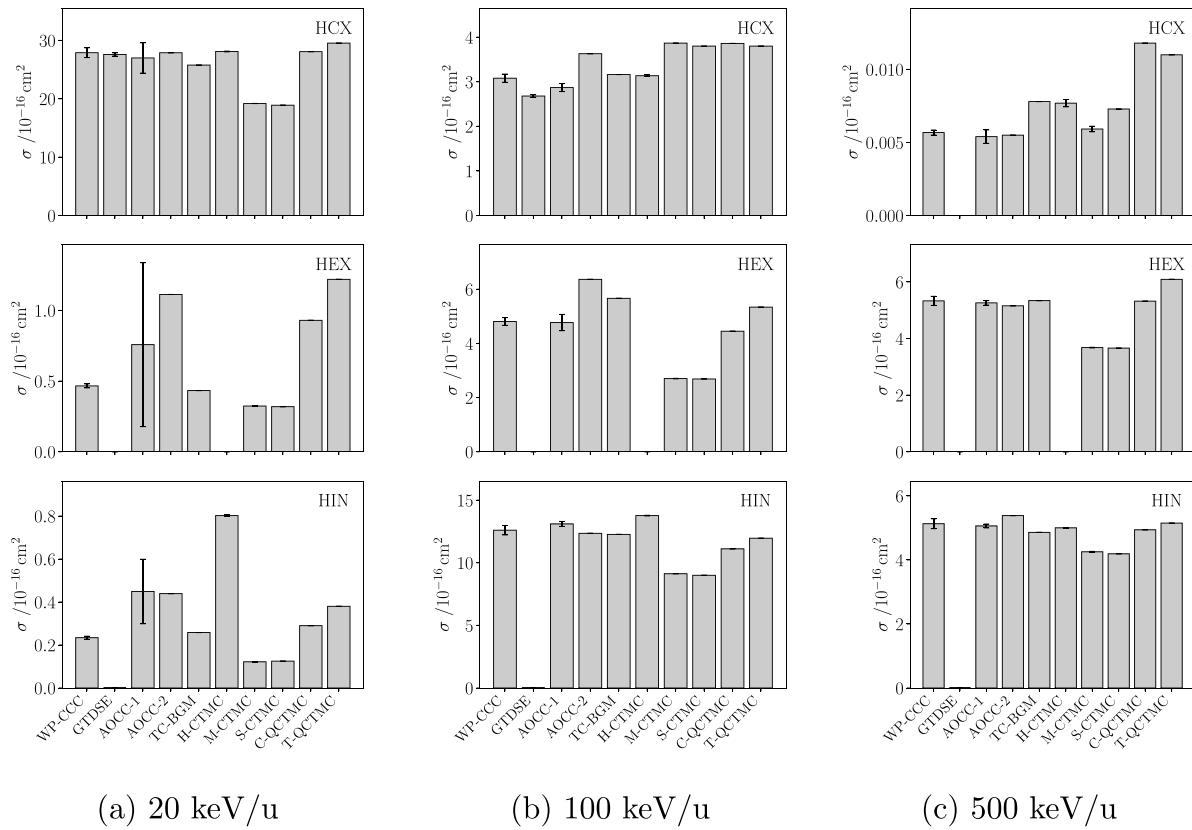
Figure 2. Comparison of computational methods for $H(1s) - Be^{4+}$ collisions for charge transfer (HCX), excitation (HEX), and ionization (HIN) processes at different energies. The WP-CCC results are from [47]. All other results: present work.

oscillating phases of the basis states for the electron transfer channels. Among the CTMC variants, in general the M-CTMC and S-CTMC methods underestimate the cross section at low energies; conversely the C-QCTMC and T-QCTMC methods overestimate the cross section at high energy. Overall, for this process H-CTMC is in reasonable agreement with the semi-classical methods at all energies.

In contrast to charge exchange, the total cross sections for excitation (shown in the middle panels of figure 2) computed with the different approaches vary significantly, particularly at 20 keV. For low energies charge exchange is the dominant channel when considering initial ground target state and the cross sections of target excitation and ionization get generally small and decrease very rapidly with decreasing energies. This may imply difficulties for convergence with respect to the size of the basis sets used in the close-coupling calculations, especially considering the range and the number of pseudo states of positive energies included in these bases. The M-CTMC and S-CTMC methods underestimate the cross section at all energies; agreement between the semi-classical methods improves with increasing energy.

The cross sections for ionization for the collisional system $H(1s) + Be^{4+}$ are shown in the lower panels of figure 2. Ionization processes are, in general, the most difficult ones to describe theoretically. However, except for the M-CTMC and S-CTMC approaches, the methods predict fairly similar cross sections, except at 20 keV, where ionization is weak.

For more detailed discussions of various aspects of $H(1s) + Be^{4+}$ collisions, see [47, 54, 86, 93].

Calculations involving excited states are significantly more challenging than the ground state as they require larger basis sets, and more extended position space and impact parameter range to converge for any theoretical approach. This, in turn, leads to a dramatic increase in computer resources needed. Figure 3 shows results obtained for bare beryllium ion scattering on atomic hydrogen in the 2s excited state at the same three impact energies as in figure 2.

Comparison of figures 2 and 3 reveals that at 20 keV u^{-1}, the total charge exchange cross section is about twice as large for Be^{4+} - $H(2s)$ collisions as for Be^{4+} - $H(1s)$ collisions. However, for projectile energies 100 and 500 keV u^{-1}, the cross section for collisions with $H(2s)$ is approximately an order of magnitude smaller than for $H(1s)$ charge exchange. For excitation and ionization, the cross section is larger for collisions with $H(2s)$ than with $H(1s)$ at all energies. The competition between ionization and charge exchange processes yields a faster decrease of the cross sections for CX from $H(2s)$ than from $H(1s)$, and this competition starts at lower energies in the case of $Be^{4+}+H(2s)$ collisions.

Excluding the AOCC results, which are associated with large uncertainties, all the theoretical methods agree to within about 15% at all energies for charge exchange with $H(2s)$. Unlike with $H(1s)$ collisions, there is little improvement in the agreement between methods at higher energies for excitation;
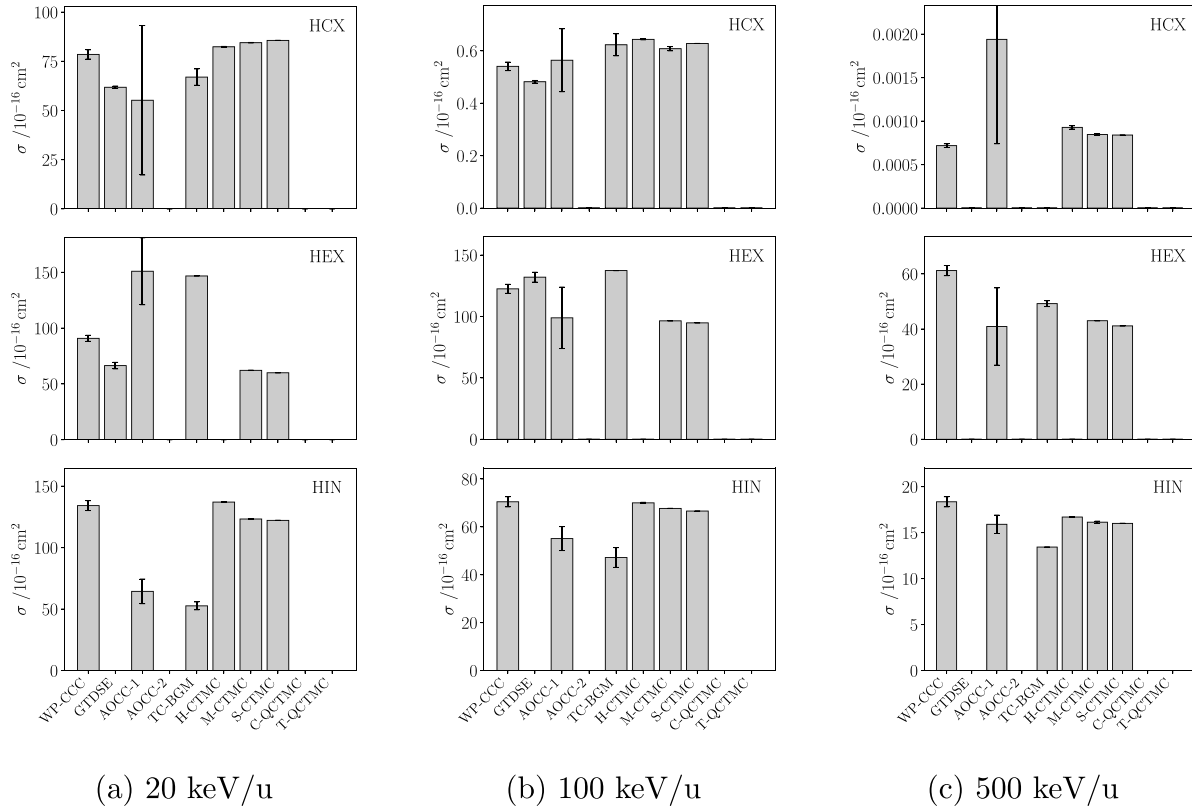
Figure 3. Comparison of computational methods for H(2s) − Be^{4+} collisions for charge transfer (HCX), excitation (HEX), and ionization (HIN) processes at different energies. The WP-CCC results are from [49, 51]. The GTDSE, H-CTMC and M-CTMC results are from [55]. All other results: present work.

the WP-CCC calculations predict cross section values about 25%–30% higher compared to other calculations.

For ionization, within the semi-classical methods agreement is generally poor, with WP-CCC consistently predicting higher cross section values than AOCC and TC-BGM; the CTMC variants agree better with each other and are closer to the WP-CCC results.

Collisions involving excited states of H were also investigated in [49, 51, 55, 72].

In summary, it is clear that the processes taking place in H(1s) + Be^{4+} collisions are fairly well understood. However, the same cannot be said about H(2s) + Be^{4+} collisions. Here the deviation between results from the different computational methods considered in this work is relatively large and no firm conclusion can be drawn concerning their quality or applicability; more calculations using alternative methods and/or experimental data are required.

4. Ionization and charge transfer for proton-hydrogen collisions

Proton–hydrogen scattering is the simplest prototype of ion–atom collisions where all collision processes, including elastic scattering and target excitation, electron capture by the projectile and breakup of the system into three free particles, take place. Despite practical difficulties in preparing atomic targets, the proton–hydrogen collision problem has been extensively studied experimentally, and there is a large amount of cross section data for excitation, ionization and charge transfer over a wide energy range. On the other hand, the rearrangement nature of the problem when the projectile can capture the target electron into a bound or continuum state has been a major challenge for the theory. A number of theoretical approaches have been developed to address the problem. Agreement between theory and experiment for the charge transfer and excitation (at least for the lowest-lying target states) is excellent. However, as one can see in figure 1, for ionization some discrepancy still remains. Specifically, at the peak of the ionization cross section, the theory developed by Kołakowska *et al* [17] overestimates the experimental data by Shah and Gilbody [10] and Shah *et al* [11] by about 35%. Kołakowska *et al* used a combination of a three-dimensional lattice solution of the time-dependent Schrödinger equation for low quantum states ($n \leqslant 3$) and classical trajectory Monte Carlo results for high quantum states ($n \geqslant 4$) in order to calculate the total electron-loss and total charge-transfer cross sections. The ionization cross section was then calculated as the difference between the latter two. The problem was later addressed using the quantum-mechanical CCC method [23] where the ionization channel was treated explicitly. The results also overestimated the experiment but the deviation was 'only' 20%. However, by
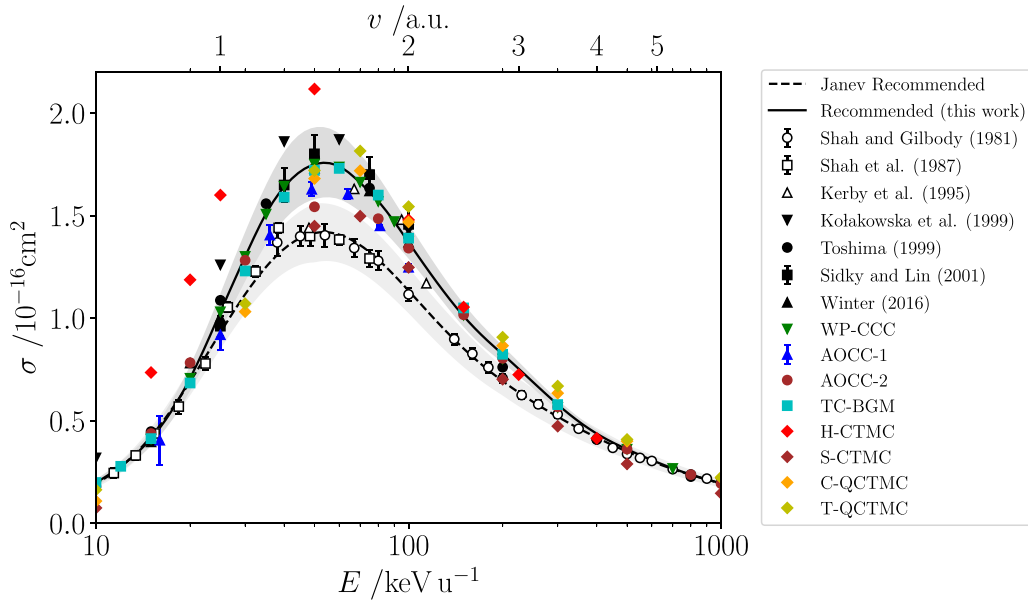
Figure 4. Experimental and calculated cross sections for proton-impact ionization of ground-state hydrogen. Solid and open black symbols are as for figure 1; dashed line with uncertainty interval band: recommended cross sections obtained from the fit function of Janev and Smith [6]. New calculations are: the WP-CCC results from [27] (this paper reported both 1-center and 2-center results; here, 2-center results are shown), the AOCC-1 results from [26], the TC-BGM results from [25], the S-CTMC, T-QCTMC, and C-QCTMC results from [84], the AOCC-2 and H-CTMC results are present calculations.

comparing the results for electron loss from the single-center and two-center calculations it was argued that even this 20% difference could not be explained.

4.1. H(1s) + p: review and recommendation of ionization cross section

To clarify the situation, the proton–hydrogen ionization problem has recently been revisited using TC-BGM [25], the single- and two-center versions of the WP-CCC method [27], two independent versions of the AOCC method [26, 60], and a few distinct implementations of the CTMC method. Figure 4 shows the energy dependence of the integrated cross section for ionization in proton collisions with hydrogen in the ground state. In addition to the experimental data and older calculations, the figure includes the results of the aforementioned new calculations. We consider the most controversial intermediate energy range between 10 and 1000 keV u^{-1}. As one can see, all recent calculations give cross sections larger than the experimental data by Shah and Gilbody [10] and Shah *et al* [11] within the energy interval from 30 to 100 keV u^{-1} which includes the peak. On a positive note, all the theories agree with the aforementioned experiments in terms of the peak position. Most of the theories appear to better support the experimental data by Kerby *et al* [12]. However, the latter is limited to five collision energies only and the peak location seems shifted to higher energy in disagreement with the theoretical predictions. In any case, all these results suggest that the Janev recommended data, shown in the figure by a dashed line, may have to be revisited. Moreover, given the fundamental nature of the scattering problem, the presented discrepancies for the ionization cross section warrant more detailed experimental

and theoretical investigations. In particular, differential ionization studies may shed further light on the problem.

4.1.1. Recommended cross section Ascribing an error bar to a collection of calculations is a matter of judgment and more so in this case since we are favoring the new calculations over measured cross sections. The experimental uncertainties were small but the cross section value was determined by normalizing to a first Born approximation cross section at 1500 keV and the error introduced by this was considered to be at most ±5% [11]. The close-coupled theoretical approaches model the intermediate energy range and do not impose any Born-like shape in this region. The agreement of a number of independent calculations further supports a shift in the recommendation. Figure 4 gives an energy dependent error bar which is consistent with the different calculations and narrows as low and high energy asymptotic behavior dominates.

The WP-CCC and TC-BGM values are used as the basis of a new recommendation with a heuristic weighting applied to the post-1993 calculations to give an envelope of uncertainty. The recommended cross section, and the upper and lower curves, are fitted to an 8-parameter fit used in [94],

$$
\sigma_{ion} = b_1 n^4 \left[\frac{\tilde{E}^{b_2} \exp(-b_3 \tilde{E})}{1 + b_4 \tilde{E}^{b_5}} + \frac{b_6 \exp(-b_7/\tilde{E}) \ln(1 + b_8 \tilde{E})}{\tilde{E}} \right]
$$
$$
(\times 10^{-16}\ \mathrm{cm}^2), \tag{37}
$$

where E is the energy in keV/u, n is the principal quantum number of the bound electron, e.g. $n = 1$ for the ground state and $\tilde{E} = n^2 E$. This function superseded that used in [6] which is the Janev recommendation in figure 4 (dashed curve). The coefficients are given in table 2.

Table 2. Value of parameters b_i of equation (37) for the proton impact ionization cross section of ground state hydrogen. Coefficients are for the recommended cross section and the upper and lower error bars.

b_i	Recommended	Lower	Upper
b_1	8.91809×10^{-6}	1.04117×10^{-5}	7.73939×10^{-6}
b_2	7.45994	6.98437	7.90962
b_3	4.61087×10^{-2}	4.53156×10^{-2}	4.69119×10^{-2}
b_4	3.94967×10^{-3}	4.19344×10^{-3}	3.68728×10^{-3}
b_5	5.41063	5.01211	5.79432
b_6	$8.88087 \times 10^{+5}$	$7.27165 \times 10^{+5}$	$1.05948 \times 10^{+6}$
b_7	$6.87898 \times 10^{+1}$	$6.90418 \times 10^{+1}$	$6.86315 \times 10^{+1}$
b_8	$6.82641 \times 10^{+9}$	$4.74658 \times 10^{+9}$	$1.19159 \times 10^{+10}$

The analytical fit imposes a shape on the cross section which differs from the recommended curve by $\sim 0.5\%$ at 100 keV but by $\sim 3.5\%$ at 200 keV. The goal is to recommend a curve for use in application so the numerical data, available via CollisionDB, is preferred when comparing different atomic data methods and measurements.

4.2. H(nl) + p: ionization and charge transfer

Figure 5(*a*) shows the cross sections for proton-impact ionization of H(2s) and figure 5(*b*) of H(2p) calculated using various methods. Unfortunately, there is no experiment to compare. As one can see, all calculations generally agree with each other with the largest deviation being at the peak of the cross section. Here the deviation reaches 20% but it is much smaller at the high energy region, e.g. the range specially important for fusion studies. So, for instance, all the points are practically within a 10% spread interval for the energy above 25 keV ($v = 1$ a.u.). The TC-BGM and AOCC-1 calculations provide literally the upper and low limit for the cross sections. At the same time, all CTMC calculations and WP-CCC data can be hardly distinguished above 50 keV u^{-1} for 2s state. We also note that in comparison to ionization of H(1s), the peak position moves to lower energy (from about 50 keV down to about 12 keV for 2s and to about 15 keV for 2p). At the same time, the magnitude of the peaks for 2s and 2p increases by about 15–20 times. Though the position and magnitude of the peak are significantly different, the shape of the cross sections remains quite similar to that for the ground state, i.e. the analytical fit can be based on the same formula (37). The new fit coefficients for the levels 2s, 2p and $n = 2$ are summarized in the table 3. The magnitude of 2p ionization is also comparable with ionization of H(2s). Results for proton-induced ionization of hydrogen initially in the $2p_0$ and $2p_1$ states were also reported in [25, 43] and are not shown here. The peak positions predicted in the TC-BGM and WP-CCC methods coincide. It is about 20 keV and 15 keV for H($2p_0$) and H($2p_1$), respectively. The magnitudes of the peaks obtained in the TC-BGM and WP-CCC methods deviate by 10%–14%, which is similar to the spread seen for ionization of H(1s) and H(2s) and can be considered acceptable.

The role of the new data for collisional radiative (CR) models should be not underestimated. Indeed, the mistake of a
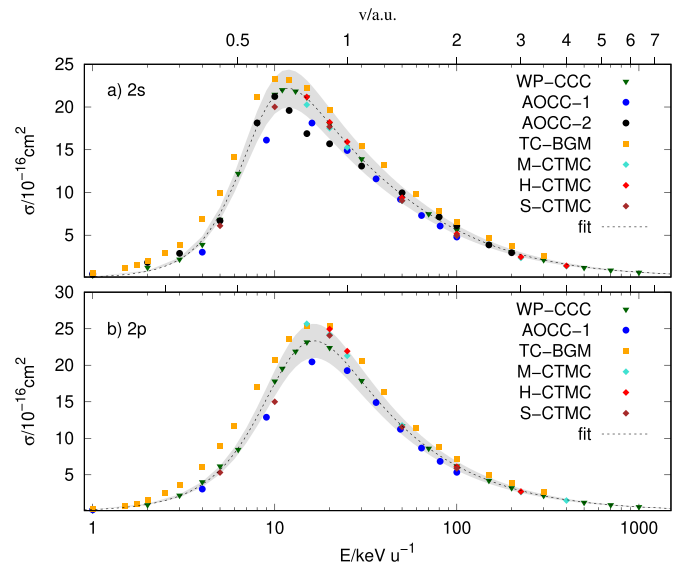

Figure 5. Theoretical cross sections for proton-impact ionization of H(2s) (*a*) and of H(2p) (*b*) calculated using different methods. The WP-CCC results are from [43], the TC-BGM results from [25], the AOCC-1 are from [26], the AOCC-2 and set of H-CTMC, M-CTMC and S-CTMC results are present calculations. The dashed curve shows the fit of the WP-CCC data and the grey region exemplifies the deviation of 10% from the fitted values.

Table 3. Value of parameters b_i of equation (37) for the proton impact ionization cross section of excited states.

b_i	2s	2p	$n = 2$
b_1	2.5299×10^{-4}	1.0025×10^{-3}	7.5944×10^{-4}
b_2	2.5346	1.9676	2.0885
b_3	5.4420×10^{-4}	2.2253×10^{-4}	4.8564×10^{-5}
b_4	1.1526×10^{-6}	2.8664×10^{-6}	5.2331×10^{-6}
b_5	3.8073	3.2075	3.1594
b_6	$5.0364 \times 10^{+4}$	$1.1339 \times 10^{+4}$	$6.3934 \times 10^{+3}$
b_7	$1.1092 \times 10^{+2}$	$1.2879 \times 10^{+2}$	$1.1080 \times 10^{+2}$
b_8	$1.4457 \times 10^{+2}$	$3.9472 \times 10^{+1}$	$2.0909 \times 10^{+4}$

factor of two in the original values of ionization cross section for $n = 2$ and $n = 3$ levels [32, 95, 96] propagated into the recommended data [6] and ALADDIN database. It resulted in incorrect values for populations of $n = 2$ and $n = 3$ levels and in the beam emission, specially at high plasma density [97]. This error was recognized and improved in a number of codes [7] and in the ALADDIN database the shape of ionization cross section was selected as a result of compilation of two sets of data (figure 2 of [98]). In the present paper, however, the new data remarkably improves our knowledge on ionization: the data from different codes remain within the error bars of 10%–20% down to 10 keV u^{-1}. Such precision was never achieved in the past. One should also take into account that at the beam energies below $20 - 30$ keV u^{-1} the main loss channel of bound electron is the charge exchange process discussed below and not the ionization by the proton impact. Figure 6 summarizes the new data for ionization cross section of $n = 2$. Here, as in the calculations for 2s and 2p levels the codes provide surprisingly good agreement for the energies
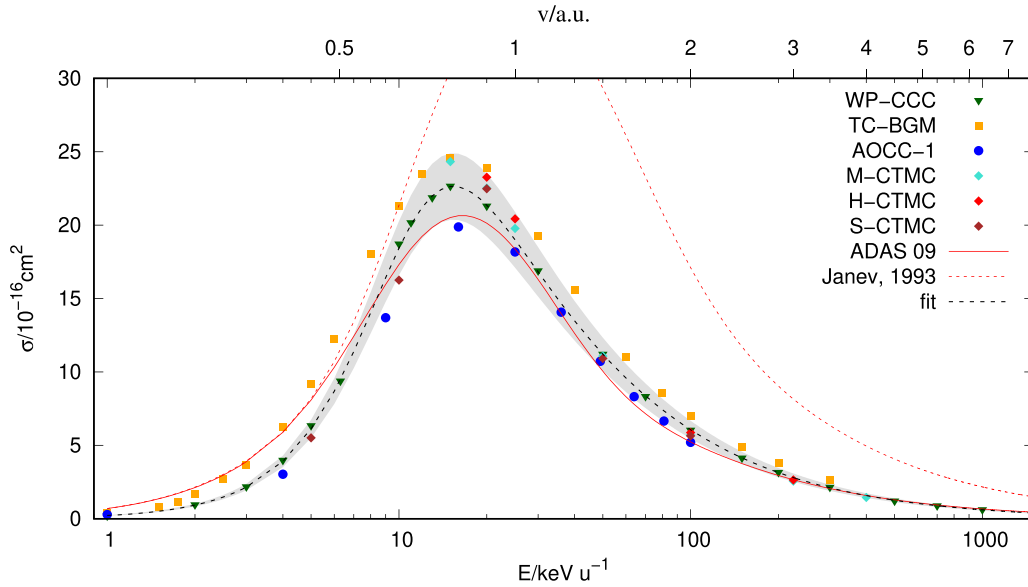
Figure 6. Cross sections for proton-impact ionization of $n = 2$ calculated using different methods. The WP-CCC results are from [43], the TC-BGM results are from [25], the AOCC-1 are from [26], and the set of H-CTMC, M-CTMC and S-CTMC results are present calculations. The dashed curve shows the fit of the WP-CCC data and the grey region exemplifies the deviation of 10% from the fitted values. The previously recommended derived data [6] are shown using red dashed line and compiled data [98] are shown using the solid red curve.
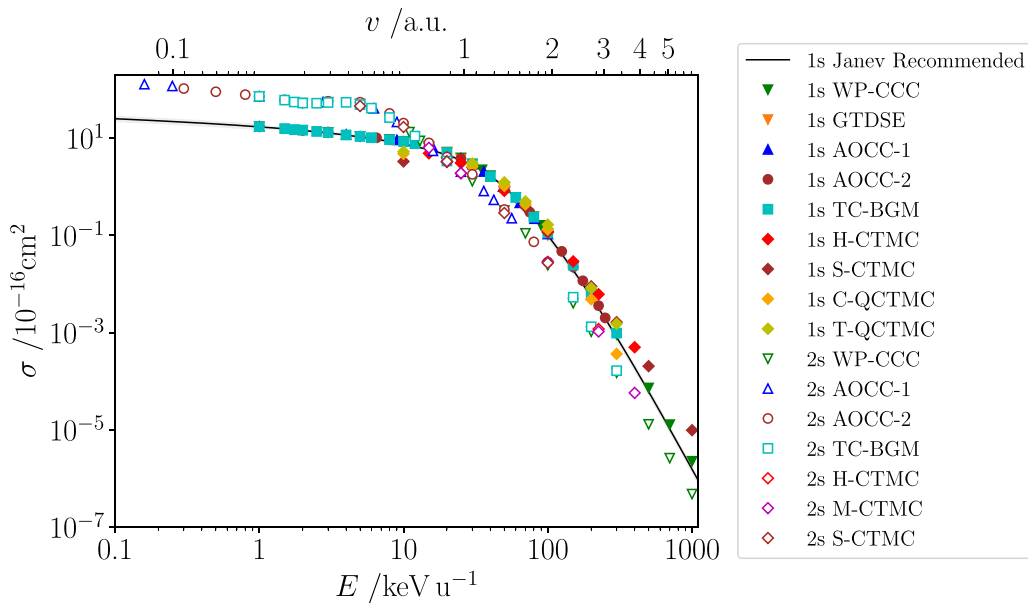
Figure 7. Theoretical cross sections for charge transfer in collisions of protons with H(1s) and H(2s). The WP-CCC results for p-H(1s) are from [27], for p-H(2s) are from [43]. The TC-BGM results are from [25] and the AOCC-1 are from [26], see also [24]. The 1s S-CTMC and the 1s C-QCTMC results are from [29, 84]. The GTDSE, AOCC-2, H-CTMC, M-CTMC, 1s T-QCTMC and 2s S-CTMC results are the present calculations. The solid black line shows the recommended cross section of Janev and Smith [6] and includes a small uncertainty interval in this region.

above 20 keV u^{-1}. The fitting coefficients [98] provide also a very good description of the data in the whole energy interval. In the low energy case one approaches the TC-BGM calculations and at high energy it approximates the AOCC-1 data. In contrast to this the Janev data [6] overestimate the cross section above 20 keV by a factor of two and more.

Figure 7 compares the theoretical cross sections for charge transfer in collisions of protons with H(1s) and H(2s). Electron capture from the ground state of hydrogen is fairly well

understood as far as the integrated total capture cross section is concerned, with practically all the methods giving pretty similar results (except for the S-CTMC and C-QCTMC methods which somewhat deviate from the rest around 10 keV and 300 keV). Moreover, these results (shown in the figure using solid symbols) are in very good agreement with experiment (available but not shown in the figure). At the same time, no experimental measurements of charge transfer in proton collisions with initially excited states of hydrogen are available.

Therefore, investigations are focused on improving the accuracy of theoretical calculations by comparing the results of various independent studies. The results are shown using open symbols. As one can see, in contrast to ionization of H(2s), the results of all the calculations are in good agreement with each other. This is due to the fact that it is much easier to reach convergence in the capture cross section than in the ionization one. One can clearly notice that below 10 keV, the cross section for capture from the 2s state is substantially larger than from the 1s state. However, around 15 keV, these two cross sections are comparable in magnitude. At higher energies, capture from the ground state dominates.

A similar situation is seen also for Be^{4+} collisions with H(1s) and H(2s) (see figures 2 and 3). According to Antonio *et al* [49], the reason for this is the difference in the radial probability distribution for finding the electron at a certain distance from the target nucleus in the 1s and 2s states. Indeed for high impact energies charge transfer is only possible for trajectories maximizing interaction time (and overlap) between target and projectile, therefore at small values of impact parameter, b, favoring initial state with electronic density closer to nucleus, i.e. 1s vs. 2s states. For a complementary explanation, one can look at the probability distributions in momentum space and argue that larger radial momenta contribute significantly to the 1s state compared to the 2s state which makes capture into a fast-moving ion easier. The concept of kinematical capture at very high energies is based on a similar argument (see, e.g. [99] and references therein).

Results for electron capture from H(2p$_0$) and H(2p$_1$) can be found in [25, 42] and [24, 26] for cross sections from H(2p), i.e. averaged over magnetic quantum numbers. These works also discuss state-selective capture and further excitation or de-excitation of the target in proton collisions with hydrogen initially in the 2s, 2p$_0$ and 2p$_1$ states.

5. Collisional atomic data in neutral beam modeling: penetration, photoemission and CXRS

Collisional atomic data play a fundamental role in investigating the efficiency of plasma heating using NB injection, beam penetration and also in providing diagnostic information on plasma parameters such as impurity concentration [100], plasma rotation and temperature [101] and measurements of the q-profile [102, 103]. The latter information is obtained from the photoemission of fast beam atoms but also the impurity ions.

Initially, the collisional atomic data as in the case of injection of hydrogen or deuterium beams were limited to ionization of ground-state hydrogen by collisions with plasma ions and electrons (figure 4). However, it was realized that the multistep collisional processes such as excitation or ionization could considerably impact the beam penetration, e.g. increase the beam stopping cross sections into the core of magnetic fusion plasma [104].

The system of coupled rate equations for population of the levels can be written [104]:

$$\frac{dN_i}{dt} = -L_i N_i + \sum_{j<i} \left(K_{ji} N_j - (K_{ij} + A_{ij}) N_i \right)$$
$$+ \sum_{j>i} \left((K_{ji} + A_{ji}) N_j - K_{ij} N_i \right) = \sum_j Q_{ji} N_j, \quad (38)$$

where L_i is the electron loss due to ionization by electron and ion impact and charge exchange on plasma ions, K_{pq} is the collisional rate of excitation if the level p lies energetically lower than the level q and deexcitation if the level p lies energetically higher than the level q; A_{pq} is the radiative transition probability between the levels ($p > q$). In the case of a Maxwellian distribution function for ions and electrons, the beam velocity is usually ignored in the calculations of electron rate coefficients (excitation and ionization by electron impact). For collisions with ions the situation is more difficult as the relative velocity between the ions and beam particles must be considered, especially for beam energies comparable to the ion temperature. For a Maxwellian distribution function of ions the expression for the rate coefficient can be given in the closed analytical form [105]:

$$K_{pq} = \frac{1}{\sqrt{\pi} u_1 u_2} \int_{\Delta u}^{\infty} u^2 \sigma_{pq}(E_r) \left\{ \exp\left[-\left(\frac{u - u_1}{u_2} \right)^2 \right] \right.$$
$$\left. - \exp\left[-\left(\frac{u + u_1}{u_2} \right)^2 \right] \right\} du, \quad (39)$$

where $u_1 = \sqrt{2E/m_1}$ is the beam velocity of the atom with the mass m_1 and the energy E and $u_2 = \sqrt{2T/m_2}$ is the most probable speed of the ion with the temperature T and the mass m_2; $\sigma_{pq}(E_r)$ is the excitation cross section between the levels p and q; u is the relative velocity between the particles connected with the energy $E_r = \mu u^2 / 2$ with $\mu = m_1 m_2 / (m_1 + m_2)$ and Δu is the threshold value. The similar expression is also applied to the ionization and the charge exchange reactions between beam atoms and ions in the loss rate L_i.

In the case of quasistatic approximation ($dN_i/dt = 0$) the system of coupled equations for beam excited levels represents a system of linear equations which can be solved for the relative populations, $n_i = N_i/N_0$, of excited levels with N_0 being the ground level population. The line intensity or the photoemission can be derived for the specific transition $p \to q$ as $\propto n_p A_{pq}$ and tabulated as a function of beam energy, ion and electron density and ion temperature or the effective plasma charge Z_{eff}. The beam-stopping cross section is obtained using the known relative population of excited levels:

$$\sigma_{BS} = \sum n_i L_i / (N_e v_b), \quad (40)$$

where N_e is the electron density and v_b is the beam velocity. Such data are available and analyzed for instance in the Atomic Database and Analysis Structures (ADAS) package [106].

Charge exchange recombination spectroscopy in tokamak plasmas is another example of application where neutral beam interaction data comes in play:
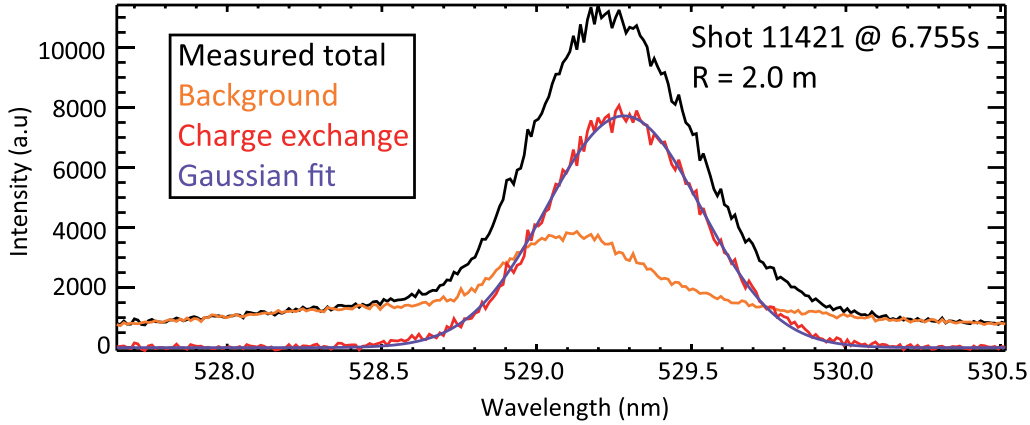
$$X^{Z+1} + H \longrightarrow X^{Z*} + H^+ \longrightarrow X^Z + H^+ + \hbar\omega. \quad (41)$$
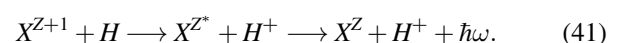
Figure 8. Charge exchange spectra with ('Measured total') and without ('Background') the neutral beam injection from the KSTAR CXRS measurement system. The active charge exchange component ('Charge exchange') is a Gaussian fit with the instrumental function whose full width half maximum is about 0.1 nm. a.u here represents arbitrary units.

While the temperature and flow velocity of the impurity particles can be inferred directly from spectral measurements without the knowledge of the cross section data [4, 5, 34, 107] the measurements of the impurity ion density X^{Z+1} in (41) requires detailed calculations on beam penetration and interaction with bulk plasma species. The expression for the population of the excited level N_i^Z from [108] is:

$$N_i^Z = N_e \left(E_i^0 N_0^z + \sum_m E_i^m N_m^z \right) + N_e R_i^0 N_0^{Z+1} + N_0 G_i N_0^{Z+1}. \tag{42}$$

Here the system of coupled equations is written for the populations N_i^Z of the impurity ions (Z) and replacing the loss term L_i in (38) by the influx rate due to the charge exchange reaction among the excited levels i of the impurity ion (Z) and the neutral beam atoms H or D with the density N_0. The vectors E_i^0, E_i^m are obtained from the inverse matrix (38) for excitation from the ground or metastable levels of the ion (Z), R_i^0 is the vector obtained from the inverse matrix for the electronic recombination and, finally, G_i^0 is the vector responsible for the active charge exchange (ACX) signal. The level populations of the ion (Z) are calculated relative to the ground level N_0^{Z+1} of the impurity ion ($Z + 1$). In the general case, however, the metastables of impurity ion ($Z + 1$) and the beam excited levels N_i also contribute to the ACX signal. The resulting photoemission, contributing at different wavelengths due to the Doppler effect, consists of sum of the passive (PCX) and active charge exchange signals. By observing the lines of low Z impurities such as He, Be, or C of H-like ions ($R_i^0 \rightarrow 0$) with high principal quantum numbers ($E_i^0, E_i^m \rightarrow 0$) one suppresses the PCX contributions making the ACX part the dominant signal. The ACX component is in addition shifted from the weak PCX one through the Doppler effect. The example of the spectra from different impurities can be found in [4, 5, 34, 107]. Figure 8 illustrates the carbon impurity charge exchange spectra measured from one of the central chords ($R = 2.0\,\text{m}$) integrated over 5 msec by the KSTAR CXRS system. The passive component measured without the neutral beam injection is subtracted

from the total spectrum and one can obtain the active charge exchange component, from which various impurity quantities can be obtained.

If the lines-of-sight in the CXRS system are tangential to individual flux surfaces as in case of the KSTAR [100] the impurity density can be given by the simple formula

$$n^{Z+1} = \frac{4\pi \epsilon_{CX}^\lambda}{\sum_k \sum_j \langle \sigma v \rangle_{j,k}^\lambda \int n_{b_{j,k}}(l) dl}, \tag{43}$$

where ϵ_{CX}^λ is the brightness of the charge exchange signal of the impurity species of interest at wavelength λ, which is obtained from the measured spectral line intensities, $\langle \sigma v \rangle$ is the Maxwellian-integrated charge exchange emission rate coefficient, and $n_b(l)$ is the neutral beam density as a function of the viewing chord's path length dl over the width of the neutral beam. The subscripts j and k represent the summations being made over the beam atom's excited levels and the beam energy fractions (full, half, and third the initially accelerated voltage), respectively. So, for example, the equation (43) was applied for the CXRS measurements in the KSTAR tokamak where the dominant impurity ion species is carbon (C^{6+}). Therefore, its dominant emission after the charge exchange with a beam deuterium atom is C^{5+} and the transition from $n = 8 \rightarrow 7$ was detected. The effective charge exchange emission rate, $\langle \sigma v \rangle$ in equation (43), represents a function of plasma density, temperature, effective charge (Z_{eff}), and beam energy at the location of the emission volume as discussed above. It should be noted that although the emission rate for the charge exchange with C^{6+} for the ground-state beam atom ($n = 1$) is smaller by about two orders of magnitude than that for the first excited state beam atom ($n = 2$), it is not negligible because the neutral beam density behaves in an exactly opposite way—that is, the $n = 1$ beam density is about two orders of magnitude higher than that of $n = 2$ (as shown in figure 9). Therefore, $\langle \sigma v \rangle$ for both $n = 1$ and $n = 2$ neutral beam atomic states need to be taken into account (subscript j in equation (43)). These data are obtained from the ADF12 files in ADAS packages,
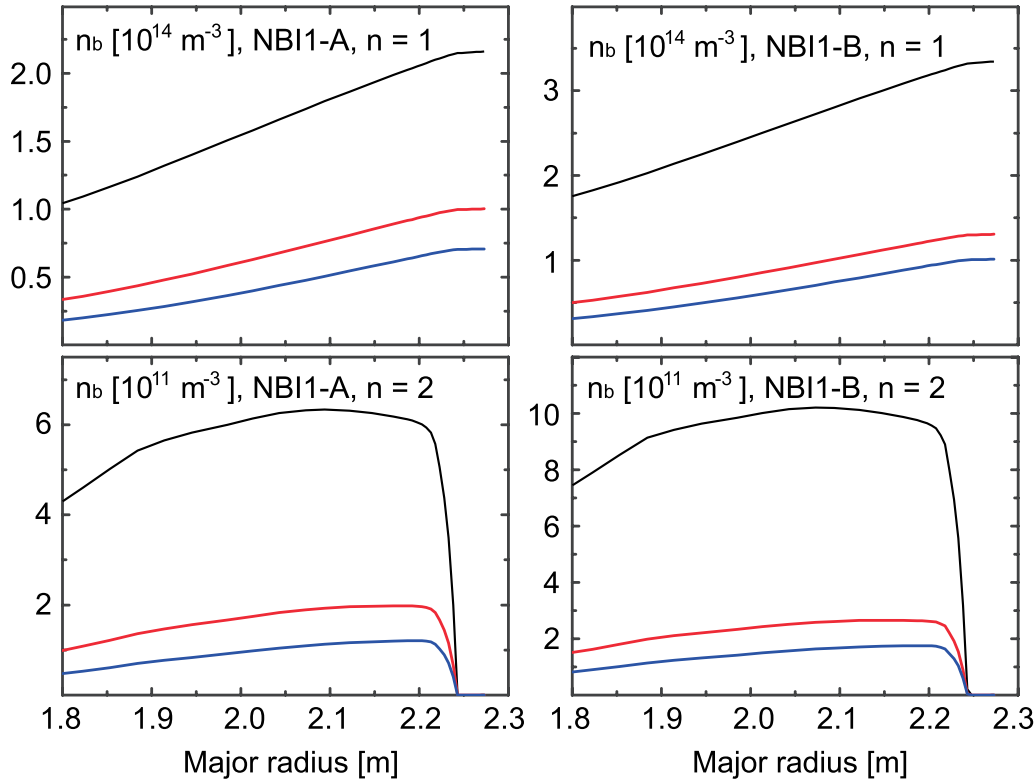
Figure 9. Radial profiles of the path-integrated neutral beam density ($\int n_{b_{j,k}}(l)dl$ in equation (43)) calculated by KSTARBEAM at ground ($n = 1$) and first excited ($n = 2$) states for the neutral beam made of two ion sources (NBI1-A and NBI1-B) injected into a typical KSTAR H-mode discharge. The full, half, and third beam energy fractions are denoted in black, red, and blue, respectively.

qef93#h_c6.dat and qef97#h_en2_kvi#c6.dat for the ground ($n = 1$) and the excited ($n = 2$) states, respectively.

The neutral beam density, n_b in equation (43), is calculated by the beam attenuation code, ALCBEAM, originally developed for the Alcator C-Mod tokamak beam penetration calculations that include three-dimensional geometry for the grid structure of the ion source, beam attenuation by neutral gas and plasma particles, and beam neutral excitation [109]. The attenuation by neutral gas (deuterium and hydrogen molecules) is dominated by ionization of the beam neutrals from the beam duct down to the edge of the plasma and its cross sections follow the empirical one given in Barnett *et al* [110]. Several options are available for the cross section data set for the beam stopping whose main processes are collisional ionization, Lorentz ionization, and charge exchange. Here we have chosen ADAS v3.1 modified by Delabie [7] for the collisional data. The same database version has been used for calculating the beam excitation populations based on a collisional radiative model. The ALCBEAM code has been modified for the beam parameters and geometry for the KSTAR tokamak (called KSTARBEAM [100]). In addition, since the KSTAR neutral beam injected into the shot of interest in this work is made by two ion-source systems aligned with slightly different injection angles (denoted by NBI1-A and NBI1-B), the integral part in equation (43) is actually the contribution from both beam sources. This means the stopping and excitation calculations should be done for each beam source and the resultant $n_{b_{j,k}}(l)$ integrated over its own path

length, *dl*. Figure 9 shows the KSTARBEAM calculations of the path-length integrated neutral beam density at ground and first excited states with the three beam energy fractions (full, half and third) for NBI1-A (80 keV) and NBI1-B (90 keV) from a typical KSTAR H-mode plasma discharge (shot #28514 at 4850 msec). The local electron temperature and density is obtained from the Thomson scattering measurements and Z_{eff} is assumed to be 2.

The top figure in figure 10 presents the impurity C^{6+} density profile inferred from equation (43) with the localized charge exchange emission rate and neutral beam density obtained in the way described above.

The error bar has been propagated from the statistical error in the raw CXRS data generated from a nonlinear least squares fit. Also included in the figure (at the bottom) are the radial profiles of the electron density and temperature at the same time point. It is observed that the impurity density is quite flat through the plasma core indicating the constant impurity pump-out due to the edge localized mode during the H-mode. It is also noted that the pedestal location agrees well between the impurity and plasma electron density profiles, the pedestal top being at around $R = 2.2$ m.

In general, the development of the collisional radiative models (38) is closely connected with the quality and availability of the collisional atomic data. This is true for beam emission calculation but also for the photoemission of CXRS reactions (41). It is, therefore, not surprising that the level *i* used in
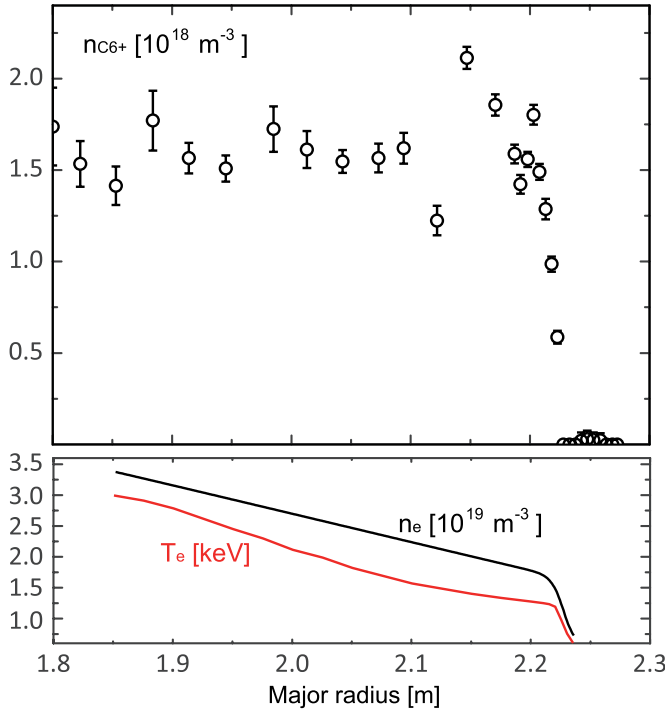
Figure 10. (Top) C^{6+} impurity density as a function of major radius for a typical KSTAR H-mode plasma, (Bottom) plasma electron density and temperature profiles measured by the Thomson scattering diagnostic system.

Figure 11. Beam emission rate coefficients for H_α and H_β lines. The beam energy is 100 keV, the ion and electron temperatures are equal to 3 keV. Bundle-nl model is shown in red and bundle-n model in blue.

the majority of the models does not really represent the *eigenstate* of the problem. So, for instance, one defines the level i either as the bundle-n level, or as the bundle-nl level by modeling the CXRS lines' emission (n and l being the principal and orbital quantum numbers, respectively.) In the first case, the populations of the fine-structure components within the same n are proportional to the statistical weights. In this approximation the collisional and radiative atomic data required for modeling are those resolved by principal quantum numbers only. In case of the CXRS spectroscopy this approximation is valid for the high plasma density and radiative transitions from the principal quantum numbers only. Due to the fact that the bound electrons observe the Zeeman-Stark effect with crossed fields in the rest frame of the ion the bundle-n model could be valid in the magnetic devices with strong magnetic field even at low ion plasma density. Whereas the static Zeeman effect and polarization of spectral components can be easily incorporated into the line shape modeling of the CXRS spectra [107], the calculation or even the criterion at which the bundle-n picture can be valid is still an open question [111]. Thus, the bundle-n situation can exist at lower plasma density compared to the calculations based on the collisional quenching due to the proton and electron impacts [112].

The bundle-nl collisional radiative model takes into account the l distribution of the charge exchange cross sections and is appropriate at low and intermediate plasma densities. For instance, the CXRS transitions from the low principal quantum numbers such as in He, Be or C cannot be adequately described without accurate nl resolved cross sections. Furthermore, the
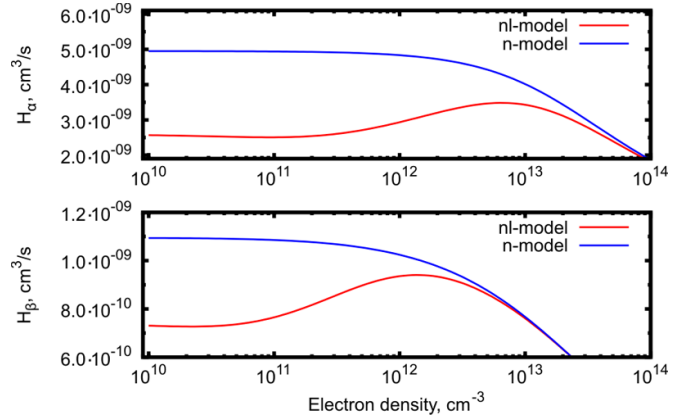
modeling of x-ray CXRS spectra ($1s^2 - 1snp$, $n \geqslant 2$) also requires the bundle-nl model [113]. In fact, the difference in the nl distributions from different calculations is immediately observed in resulting rates and finally the brightness [114]. The density-dependence of the effective rate coefficients collected, for instance, in the ADAS database is a result of collisional quenching primarily due to the heavy particle collisions within the same principal quantum number [112, 115]. The redistribution between the different principal quantum numbers occurs at electron densities which are not relevant for fusion. In the limit of high plasma density the result of the bundle-nl model must agree with the result of the bundle-n model as the populations become proportional to the statistical weights [116]. This fact is valid for CXRS spectroscopy and also for beam emission. Figure 11 shows an example of calculations [117] of the beam emission of H_α and H_β lines. At low plasma density (the coronal limit) the difference between the two models is about 30%–50%, however by increasing the density to the value of 10^{13} cm^{-3} the difference disappears for the H_β line and remains only about 10% for the H_α line. The figure exemplifies the fact that the levels belonging to the larger principal quantum number approach local thermodynamic equilibrium (LTE) at lower plasma densities [118]. It should be noted, however, that bundle-nl models seldom extend towards very high quantum numbers: firstly, the atomic data are rarely available for the principal quantum numbers above 20–30 for the CXRS problems; secondly, the Zeeman-Stark effect leads to additional quenching between the levels. One usually introduces the transition between the bundle-nl and bundle n models within the latter models [108, 112].

The bundle-nl model applied to the beam atoms in fusion plasma contains a numerical pitfall. The populations calculated within the bundle-nl model can be meaningless as, for instance, the metastable level $2s_{1/2}$ does not exist in the plasma: the coupling between the 2s and 2p levels occurs already at an electric field of $\approx 10^3$ V cm^{-1} [119]. In the case of neutral beam injection into the confined plasma, the translational or motional electric field observed by the bound electron
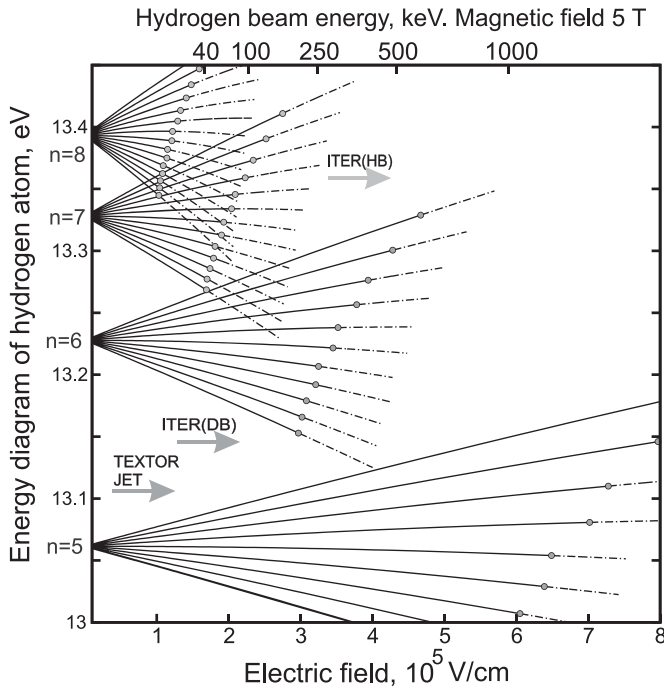
Figure 12. Energy diagram of the excited levels for beam atoms in the plasma. The energy level calculations were done in second order perturbation theory. The calculation of the ionization rates were performed using approximation [120]. The strength of electric field ($F = v \times B$) observed or expected by bound electron in the rest frame of the beam atom in the experimental conditions of tokamaks JET, TEXTOR or for ITER diagnostic (DB) and heating beams (HB) are shown as arrows. Reproduced from [121], with permission from Springer Nature.

in the rest frame of the atoms is in the range of $\approx 10^5$ V cm^{-1}. Thus, the excited levels of beam atoms can be well described using the linear Stark effect. The most accurate description of populations and emission of the beam atoms represent the parabolic quantum numbers within the frame of perturbation theory, e.g. the linear Stark effect for hydrogen atoms. This description is accurate for the principal quantum numbers up to $n = 5$–7. For higher n states the magnetic levels disappear due to field or Lorentz ionization [120]. Figure 12 shows the energy diagram of excited levels for conditions relevant to fusion plasmas as a function of electric field, which is proportional to the velocity of the beam atoms. So, for instance, for the states with $n > 6$ the ionization induced by electric field plays the dominant role—these states become quasi-continuum ones. The condition at which the field ionization rate equals to the radiative one is shown as the grey points in this figure.

Figure 12 shows that the modeling of populations of beam *eigenstates* becomes a nontrivial task as one must incorporate in the model collisional atomic data for the transitions between states with different magnetic quantum numbers. Whilst the structure calculation for atoms in electric field represents a more or less solved problem [119], the corresponding atomic data for collisional processes were until recently unavailable. The first description used two state approximations such as those of Born or Glauber [112, 122]. It was

shown, for instance, that the cross sections between the magnetic levels have a very strong dependence on the mutual orientation between the vector of electric field and the beam velocity. In the last few decades it was demonstrated that the cross sections among the parabolic quantum numbers could be represented as the linear combination of the coherent terms of the density matrix elements [8, 123]. Such representation finally provides users with the possibility to transfer the calculation from the simple approximations (Born, Glauber, eikonal, etc) to a modern theoretical approach [124]. In this case the density matrix elements for excitation, ionization and charge exchange must be known.

Obviously, MSE measurements at the plasma edge must include the time-dependent situation in its analysis. In sensitive polarization measurements the Zeeman-Stark effect for MSE components must also be considered [103, 125].

The steady state calculations (38) for the beam emission and CXRS spectroscopy allow one to prepare effective rate coefficients and look-up tables for line intensities independent on the initial conditions. In the case of neutral beam injection the population of all excited levels equals to zero whereas the population of impurity ions is prescribed by the existing coronal transport equilibrium at the time of neutral beam injection. In case of CXRS diagnostics a simple two zone model was applied to study the temporal evolution of excited levels [112]. It shows that the highly excited *nl* levels reach the quasi-steady state conditions within a few nanoseconds, so that the line-integrated CXRS signal is hardly affected during this fast transition region. The modification of the ground level population of impurity ions due to the neutral beam injection occurs on the time scale of ≈ 100 ms. In the first case the time scale is defined by the radiative loss rates; in the second case it is the collisional loss rate, which is proportional to the plasma density.

A different situation exists for the MSE diagnostic. The beam passes the distance of 5–10 cm in the plasma before the excited magnetic levels with $n = 2, 3$ or 4 reach the quasi-steady state approximation as shown in figure 13. Such distances correspond to the product of the lifetime of excited levels and the beam velocity. The beam emission would consequently be reduced.

5.1. Code comparison of the beam penetration and photoemission

In the course of the CRP, a beam penetration and photoemission benchmark was executed with a large number of participating codes and different approaches to treating the atomic data. The purpose of the benchmark was twofold. First, to evaluate the collisional radiative models (CRM) from the perspective of the applied atomic data, the required complexity and the treatment of missing atomic data. Second, to verify correct implementation and explore the applicability of different physics models to physics modeling tasks of different nature.

The participating codes apply different levels of detail and methodology to solve the governing rate equations: RENATE [127], RENATE-OD [128],
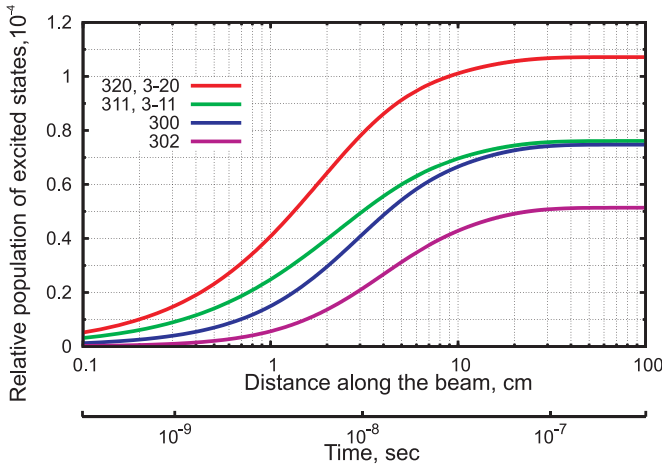
Figure 13. Non steady state calculations for the $n = 3$ populations of excited levels in the beam atoms. The levels are denoted as $nk|m|$, where m is the magnetic quantum number, $k = n_1 - n_2$, where n_1 and n_2 are the so called parabolic quantum numbers ($n_1, n_2 \geqslant 0$) and $n = n_1 + n_2 + |m| + 1$. The calculations are performed for the beam energy of 50 keV and the beam density of 10^{13} cm^{-3}. Reprinted from [126], Copyright (2010), with permission from Elsevier.

BBNBI [129], FIDASIM [130], CHERAB [131] and CRM by Marchuk [126]. The effect of the underlying physics approaches on beam attenuation and emission has been analyzed in previous publications [132, 133]. The most important conclusions are summarized as follows.

Codes such as RENATE and RENATE-OD feature a direct rate-equation solver numerically integrating the system of equations (38), which computes the valence electron distribution on various excited atomic states along the beam. Both codes feature atomic physics models with bundled-n approach for hydrogenic beams featuring cross sections based on Janev and Smith [9] with corrections from ADAS [98] and Johnson [134]. Furthermore, the collisional radiative model assumes a finite number of atomic levels and neglects higher excited states leading to a net underestimation of total beam attenuation due to omitting multi-step ionization involving higher than $n = 6$. A notable difference between RENATE and RENATE-OD lies in the handling of impurities. While RENATE uses a Z_{eff}-based approach to consider a single averaged impurity species [135], RENATE-OD considers each plasma component separately. FIDASIM uses a similar approach as above, with a notable difference in the handling of levels higher than the ones properly considered in the solving of the rate equations: FIDASIM calculates with excitation to higher levels as losses implying instantaneous further ionization. This results in a slight overestimation of ionization losses and, thus, higher beam attenuation. All further codes in the benchmark used the quasi-static approximation resulting in effective beam-stopping cross sections (40), and effective emissivities calculated in a similar manner. The difference between such codes lies in the source of such data and their implementation into beam modeling. CHERAB uses a deterministic model of beam attenuation, whereas BBNBI utilizes

a Monte-Carlo method for beam modeling, that introduces a stochastic scatter of beam properties.

Two types of test cases were formulated: the 'constant profile' test cases were to assess the attenuation rates in different plasma compositions, while the 'plasma profile' test cases were to study the effect of the different modeling approaches on realistic scenarios of beams penetrating plasmas from the aspects of both beam attenuation and photoemission. The 'constant profile' test cases featured homogeneous plasma with constant parameters. For most codes, this technically meant step functions in density and temperature, which required the elimination of the transient initial stage from the analysis. Test cases were set up to study the effects of finite temperature, different main ion species, trace impurities, and finally, multi-component plasmas. All participating codes have shown good agreement (within about 5%) in the attenuation calculations for the most common scenario of a hydrogen beam penetrating a pure hydrogen plasma, but significant deviations were found in the treatment of impurities, with no code being able to properly calculate for tungsten impurities. The benchmark has also highlighted a shortcoming in rate coefficient integration by the formula (39) of RENATE when calculating for very high energy beams (above 500 keV), so a new integration scheme was implemented in RENATE-OD to solve the problem.

From among the 'plasma profile' test cases, a case with ITER-like profile evolution featuring a large scrape-off layer blob has shown the most significant differences. All codes produced very similar attenuation rates, but the difference between rate-equation-solvers and the quasi-stationary approach became apparent in the emission profiles. While the emissivity calculated by CHERAB using the quasi-stationary approach followed exactly the density evolution of the plasma density, RENATE, RENATE-OD and FIDASIM have produced results with significantly delayed emission. The emission response calculated by FIDASIM was a bit more rapid, as expected from the difference of treating high levels of excitation.

The beam penetration and photoemission benchmark contributed to the development of participating codes and reinforced the understanding of the applicability of different modeling approaches [132, 133]. A more detailed publication on the benchmark is foreseen in the future.

5.2. Error propagation on HIN processes to modeling codes

An important goal in quantifying the uncertainty in fundamental atomic cross sections is to bound the range of quantities which depend, either directly or indirectly, upon the process. The principal atomic process which attenuates high energy neutral beams in magnetically confined fusion plasmas is ionization of the beam atoms by thermal protons in the plasma. The new calculations reported here are separately converged within the confines of their method but also collectively converge on values higher than the current recommendation. As seen in figure 4 the greatest spread is at the energy of the
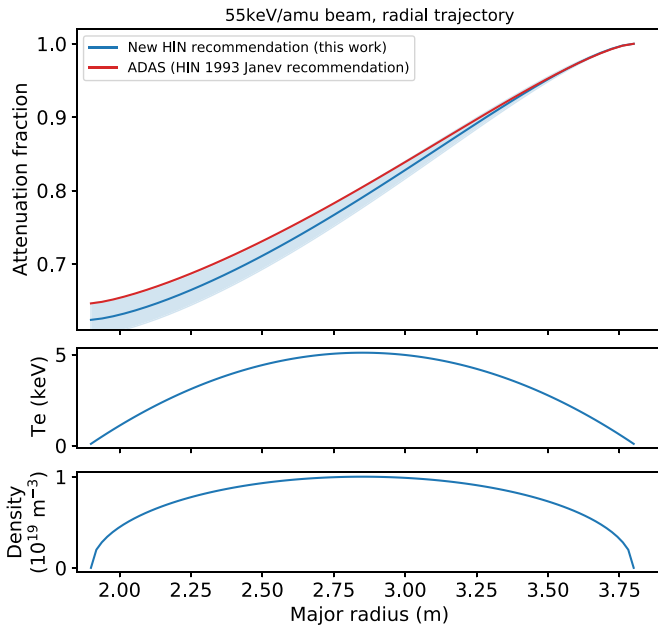
Figure 14. A simple, pencil-like, neutral beam launched into JET-like conditions shows the growing nature of attenuation and the difference between the same model when just the proton-neutral hydrogen ionization cross section is changed.

peak of the cross section ($\sim$50 keV) which corresponds to the typical energy of tokamak neutral beam systems. The recommendation of [6] was strongly influenced by the measurements of [10, 11] which had a relatively small error bar. We assess the new results by forming a new recommendation and comparing an attenuation profile which highlights the different facets of error/uncertainty, namely the effect of propagating the spread of the new data and the difference between the new and older recommendations.

The ADAS evaluation of beam stopping coefficients [2] is used to explore the consequences of the new proton impact ionization recommendation. This collisional radiative model includes direct and multi-step ion and electron processes and has been modified to propagate errors, in a Monte Carlo fashion, simultaneously in all processes. To demonstrate the importance of this process we just propagate the uncertainty in this cross section and apply the resulting stopping coefficients to a pencil-beam in JET-like conditions. A normal distribution

of values over the width given in figure 4 for each energy was applied until a Gaussian fit of the resulting set of stopping coefficients returned a mean value within 0.01% of the unvaried value. The error bar in the stopping coefficient was taken as the FWHM of the fit.

Figure 14 shows the widening attenuation profile for a 55 keV neutral beam launched into a plasma with a central temperature of 5 keV and central density of 10^{19} m^{-3}. As the new recommended cross section is larger, the resulting shine-through is lower by $\sim$5% with a spread of a similar size. It is notable that the older recommendation is not contained within the propagated error envelope of the new recommendation. The nature of an attenuation calculation results in a growing error so the magnitude/precision of the recommended error is a consequential quantity.

6. Storing and transmitting fundamental collisional data: CollisionDB and ALADDIN2

CollisionDB [136] is a database of plasma collisional processes developed at the IAEA to provide access to atomic and molecular (A + M) data relevant for fusion research and development. In practice, there are several existing databases [137–139] that aim to provide such data for different communities, including the IAEA's ALADDIN (A Labeled Atomic Data INterface) database [140]. However, these data services contain a limited amount of data concerning state-resolved collisions and do not expose an Application Programming Interface (API) for obtaining data from modeling codes in a standardized way; this functionality is provided by CollisionDB. Furthermore, the need to collect and compile fundamental collisional data to understand the plasma behavior is well recognized; to meet this need, CollisionDB offers a standardized and easy-to-use input format in which researchers can provide their data, with full attribution and metadata descriptions. In this way, CollisionDB facilitates the exchange and long-term curation of *any* A + M collisional data published in peer-reviewed resources.

An example dataset relevant to the neutral beam modeling is given below, followed by a brief description of the mandatory metadata keys. The file consists of metadata, in JSON format, followed by a separator line, followed by the numerical data itself, in white-space delimited columns.

```
{"qid": "D76333",
"reaction": "Be+4 + H 1s \u2192 Be+3 + H+",
"process_types": {"HCX": "Charge Transfer"},
"data_type": "cross section",
"refs": {"B20": {"doi": "10.1088/1361-6455/ac22e1"}},
"comment": "Total cross sections for electron capture for collision of bare Be ions
    with atomic H",
"method": "CCC",
"columns": [{"name": "E",
             "units": "eV.u-1"},
            {"name": "sigma",
             "units": "cm2"}],
"unc_perc": 3.0,
"frame": "target",
"metadata_version": "M1.0",
"time_added": "2022-05-26 11:05:42.827646+00:00"
}
------------------------------------------------------------------
1.000e+03 3.74e-15
5.000e+03 3.34e-15
1.000e+06 2.53e-20
```

Listing 1. An example CollisionDB data set file.

- A reaction represents a collision process between species, where both species and reaction are described by the conventions of the PyValem library [141].
- Each collision process is specified by a three-letter code according to the standardized schema developed for the classification of processes in plasma physics at the IAEA [142], e.g. EIN = ionization, HEX = excitation, where the prefixes 'E' and 'H' represent electron and heavy particle collisions, respectively.
- CollisionDB can currently store three types of collisional data, viz., 'cross section', 'differential cross section', 'rate coefficient'.
- The publication DOI is used to retrieve the bibliographic data through the reference management library [143, 144].
- The method can be specified as one of the pre-defined abbreviations that identify the computational method used, or as one of the following: 'experiment', 'semi-empirical' or 'estimate'.
- The columns provide an explanation of the name of the numeric data columns and its units.
- The frame represents the energy frame of reference for colliding reactants.
- Other optional metadata keys such as `threshold`, `comment`, `unc_perc`, etc, can also be attached to each dataset, as appropriate.

For full documentation and more information about basic metadata and other resources, see the site https://amdis.iaea.org/db/collisiondb/.

At the time of writing the CollisonDB hosts 122 352 datasets, mostly involving state-resolved transitions for collisions of electrons and heavy particles with atomic and molecular species. Where available, these datasets also contain the originally published fit coefficients along with cross sections or rate coefficients and the corresponding fit functions are provided in the Python language. These datasets can be queried for a set of relevant attributes, including reactants, products, author, publication DOI, general method, data type and process types. Reactants or products can be searched for atomic and molecular species (e.g. Be, Be+, H-, H2, D2) including electron (identified by e or e-), and photon (hν or hν) as well as atomic and molecular quantum states such as atomic configuration (e.g. 1s2.2s), atomic term symbol (e.g. 1S), molecular term symbol (e.g. 1Σ+g or 1SIGMA+g), individual quantum numbers as key-value pairs (e.g. n = 3), etc. Datasets that match the search query will be listed and can be downloaded as an archive or as a single record. Details of an individual collisional dataset can also be viewed along with an interactive graphical data display on the user interface.

The database is updated regularly with new data from published sources. However, the task of extracting data from the literature is not straightforward, which hinders the maintenance of these databases. Most of the data hosted in CollisionDB so far has been provided either by participants in IAEA's CRPs[18] that produce data for specific fusion research needs, or by research groups within the Global Network for

---

[18] IAEA website (available at: https://amdis.iaea.org/CRP/) (Accessed 8 September 2023).

Atomic and Molecular Plasma Physics (GNAMPP)[19] established to promote collaboration and communication between data providers and user communities. Our strategy for the long-term maintenance of CollisionDB has been to promote the submission of data in the designed schema through the IAEA's Atomic and Molecular Unit's activities and improve this prototype service based on feedback from data providers and users.

The older ALADDIN database [140] has been used as a repository for data evaluated during coordinated data activities at the IAEA's Atomic and Molecular Data Unit. These data are usually associated with publication in the IAEA Atomic and Plasma–Material Interaction Data for Fusion journal series [145], and some data sets have been recommended by these publications for use in specific fusion applications. ALADDIN has been updated to ALADDIN2[20] with the same data models and web interfaces as for CollisionDB. The old ALADDIN database contains 21 607 datasets for atomic and molecular collisional processes, while 15 902 datasets with reliable metadata and provenance have been transferred to ALADDIN2. These datasets have been processed to store the metadata according to the standardized schema explained above to ensure higher data quality and easy accessibility.

This unique compilation of atomic and molecular collisional data with structured metadata provides useful data for fusion and other areas of plasma research, and also offers opportunities for machine learning applications. For example, data from various sources can be retrieved and analyzed, which is an important aspect for evaluation purposes and uncertainty assessment. To this end, a Python package, 'PyCollisionDB' [146] has been made available to access the CollisionDB API from modeling and other codes.

7. Conclusions

The first database of cross sections for collisions of hydrogen atoms with electrons, protons and multiply charged ions appeared about 30 years ago [6]. For many years this comprehensive set of data has been widely used in magnetic fusion plasmas. Modeling the beam plasma interaction or the development of the active beam plasma diagnostics relied to a great extent on the numbers given in this data collection. In this paper, we have reviewed the *state-of-the-art* collisional data for excitation, ionization and charge exchange processes in view of the significant progress of numerical computational techniques over the last three decades. At the same time, there is a much deeper understanding of the role, structure and problems of the collisional radiative models using heavy particle collisions.

There is no doubt, that ionization of hydrogen atoms by proton impact in the impact energies range of 10–$100\,\mathrm{keV\,u^{-1}}$ represents the most challenging and crucial task. Indeed, the heating of the plasma core to conditions relevant to fusion reactions depends entirely on the production of highly energetic ions as a result of the beam atom ionization. Also, plasma diagnostics depend on the attenuation of the beam inside the plasma volume. Therefore, it is not surprising that the calculation of the ionization cross section represented the principal problem addressed in this paper. The calculations were performed using the methods such as WP-CCC, GTDSE, AOCC, TC-BGM, H-CTMC, S-CTMC and Q-CTMC described in section 2. Practically all the codes demonstrate the ionization cross section to be about 30% higher than the experimental data of Gilbody and Shah [10, 11] around its maximum at around $50\,\mathrm{keV\,u^{-1}}$. These experimental measurements were used as a basis for the recommended curve given in [6] and this significant difference has two important consequences. First, one obtains stronger beam attenuation in the plasma as expected. Second, the signal of the beam-aided diagnostic in predictive modeling is reduced due to the strong *e*-folding length in high-density plasma discharges (see for instance figure 14). In fact, the problem related to the beam attenuation at JET was already described in [7] and enhancement of the proton ionization cross sections by 30% removes to a great extent the discrepancy observed in experimental data.

Comparison between the different methods also shows rather good agreement in the cross section for ionization of hydrogen atoms in excited levels such as H(2*s*). The deviation in the peak of the cross sections between the methods remains in the order of 10%–15%. In the case of charge-exchange collisions, the rapid convergence in calculation stimulates very good agreement in the data obtained for p+H(1s) and p+H(2s) collisions. In addition, a detailed comparison was performed for the collisions of multiply charged ions and hydrogen. The system of study was $Be^{4+} + H$ for the energies of 20, 100 and $500\,\mathrm{keV\,u^{-1}}$. In this case, the majority of the codes also show much better agreement for the charge-exchange reaction in comparison to ionization and excitation channels. The spread in the excitation and ionization data is less pronounced in the case of the 100 and $500\,\mathrm{keV\,u^{-1}}$ calculations in comparison to the $20\,\mathrm{keV\,u^{-1}}$ case. For the case of collisions involving atoms in excited level H(2*s*), the data show rather poor agreement between the different codes demonstrating the deficits in the description and number of the resulting channels.

Comparison of plasma codes incorporating the collisional atomic data was also performed in this paper. Different codes used in plasma physics were applied to explore the beam attenuation and emission relevant to fusion plasma. The conditions were varied from the constant profiles to realistic ones expected for ITER. One should note, however, that the codes operate in different environment. While some of them are extensively used as a part of complex Monte Carlo plasma codes calculations, others were dedicated to provide populations of excited levels based on the latest results in collisional atomic physics. The majority of codes show rather good agreement in the hydrogen and deuterium plasma. The deviation between them

---

[19] IAEA website https://amdis.iaea.org/GNAMPP (Accessed 8 September 2023).

[20] IAEA website https://amdis.iaea.org/db/aladdin/ (Accessed 8 September 2023).

is at the level of 10%–15%. The presence of impurities, however, leads to significantly different results. Obviously, the new set of collisional atomic data generated in this paper increases the beam attenuation to a level far beyond the results of previous calculations based on the data [6].

Acknowledgments

Appendix. Summary of data calculated during the CRP

Table A1. Summary of total and/or state-resolved cross sections calculated during this IAEA Coordinated Research Project on Atomic Data for Neutral Beam Modeling: excitation (Exc), ionization (Ion), charge exchange (CX) involving the reactants relevant to heating and diagnostic neutral beams in fusion plasmas. Further information can be found in the references in the bibliography.

Reactant 1 (Energy range)	Reactant 2 (Energy range)	σ^{Exc}	σ^{Ion}	σ^{CX}
H(1s) 10 keV–1 MeV	H^+	[26, 27, 46, 84, 147, 148], [25]*	[23, 26, 27, 84, 124], [25]*, Present[a,b,c]	[23, 24, 26, 27, 29, 46, 84, 124, 147, 148], [25]*, Present[c,d]
	He^{2+}	[26, 44, 149]	[26, 44, 150]	[26, 29, 44, 149, 151]
	Li^{3+}	[65]*, [26, 152]	[65]*, [26, 52]	[65]*, [26, 29, 52]
	C^{3+}	[65]*	[65]*	[65]*
	O^{3+}	[65]*	[65]*	[65]*
	Be^{4+}	[86], Present[a,b,c]	[54, 86], [47]*, Present[a,b,c]	[29, 54, 86–88, 153], [47]*, Present[a,b,c,d]
	B^{5+}			[29]
	C^{5+}		[91]	[91]
	C^{6+}		[42, 79]	[29, 42, 79, 154, 155]
	N^{7+}		[79]	[29, 79]
	O^{8+}			[29]
	Ne^{10+}		[50]	[50, 60]
	H(1s)	[90, 92, 156–158]	[85, 89, 92, 159]	[85, 89, 92, 157, 159, 160]
	H_2	[73]	[73]	[73]
H($2s$, $2p_0$, $2p_1$) 10 keV–1 MeV	H^+	[26, 36], [25]*	[26, 36], [25]*,	[24, 26, 36], [25]*
	He^{2+}	[26]	[26]	[26]
	Be^{4+}	[51, 55, 72], Present[a,b,c,d]	[51, 55, 72], Present[a,b,c]	[49, 55, 72], Present[a,b,c,d]
	C^{6+}		[79]	[79]
	N^{7+}		[79]	[79]
	H(1s)	[92]	[92]	[92]
H($n > 2$)	H^+	[26]	[26]	[24, 26]
	He^{2+}	[26]	[26]	[26]
He ($1s^2\,{}^1$S)	bare ions $E_{tot} \leqslant 70$ keV	[45, 53]	[45, 53]	[45, 53, 59, 161, 162]
He ($1s2s\,{}^3$S)	bare ions $E_{tot} \leqslant 70$ keV	[163, 164]		[163, 164]
Li ($2s$)	bare ions $E_{tot} \leqslant 50$ keV	[27, 48, 165]	[27, 48]	[27, 48, 166]
Na ($3s$)	bare ions $E_{tot} \leqslant 50$ keV	[48]	[48]	[48, 167]
K ($4s$)	H^+ 1 keV–1 MeV		[48]	[48]

Superscript (*) implies that the data has been made available in CollisionDB. Present represent the data reported in this work and superscript represent the calculation method: *a*—AOCC, *b*—TC-BGM and *c*—H-CTMC and/or M-CTMC and *d*—GTDSE.

ORCID iDs

C. Hill https://orcid.org/0000-0001-6604-0126

Dipti https://orcid.org/0000-0001-6675-8509

K. Heinola https://orcid.org/0000-0002-0601-8274

N. Sisourat https://orcid.org/0000-0002-8567-5263

A. Taoutioui https://orcid.org/0000-0002-4943-5529

K. Tőkési https://orcid.org/0000-0001-8772-8472

I. Ziaeian https://orcid.org/0000-0002-0269-1429

C. Illescas https://orcid.org/0000-0001-7141-8461

L. Méndez https://orcid.org/0000-0003-1391-2634

A.S. Kadyrov https://orcid.org/0000-0002-5804-8811

N.W. Antonio https://orcid.org/0000-0003-3900-6197

A.M. Kotian https://orcid.org/0000-0001-7770-7408

T. Kirchner https://orcid.org/0000-0002-6644-3379

A.C.K. Leung https://orcid.org/0000-0001-6243-884X

J. Ko https://orcid.org/0000-0002-5501-3939

J.K. Lee https://orcid.org/0000-0002-1252-7075

O. Marchuk https://orcid.org/0000-0001-6272-2605

M.G. O'Mullane https://orcid.org/0000-0002-2160-4546

O. Asztalos https://orcid.org/0000-0002-5734-4635

L. Liu https://orcid.org/0000-0001-7816-4804

References

[1] Han H. *et al* 2022 *Nature* **609** 269–75
[2] Anderson H., von Hellermann M.G., Hoekstra R., Horton L.D., Howman A.C., Konig R.W.T., Martin R., Olson R.E. and Summers H.P. 2000 *Plasma Phys. Control. Fusion* **42** 781–806
[3] Levinton F.M., Fonck R.J., Gammel G.M., Kaita R., Kugel H.W., Powell E.T. and Roberts D.W. 1989 *Phys. Rev. Lett.* **63** 2060–3
[4] Isler R.C. 1977 *Phys. Rev. Lett.* **38** 1359–62
[5] von Hellermann M.G. *et al* 2005 *Phys. Scr.* **2005** 19
[6] Janev R.K. and Smith J.J. 1993 *Atomic and Plasma–Material Interaction Data for Fusion* vol 4 (International Atomic Energy Agency)
[7] Delabie E., Brix M., Giroud C., Jaspers R.J.E., Marchuk O., O'Mullane M.G., Ralchenko Y., Surrey E., von Hellermann M.G. and Zastrow K.D. (JET Contributors) 2010 *Plasma Phys. Control. Fusion* **52** 125008
[8] Marchuk O., Ralchenko Y. and Schultz D.R. 2012 *Plasma Phys. Control. Fusion* **54** 095010
[9] Wolfrum E., Aumayr F., Wutte D., Winter H., Hintz E., Rusbüldt D. and Schorn R.P. 1993 *Rev. Sci. Instrum.* **64** 2285–92
[10] Shah M.B. and Gilbody H.B. 1981 *J. Phys. B: At. Mol. Opt. Phys.* **14** 2361
[11] Shah M.B., Elliott D.S. and Gilbody H.B. 1987 *J. Phys. B: At. Mol. Opt. Phys.* **20** 2481
[12] Kerby G.W., Gealy M.W., Hsu Y.Y., Rudd M.E., Schultz D.R. and Reinhold C.O. 1995 *Phys. Rev.* A **51** 2256–64
[13] Park J.T., Aldag J.E., George J.M. and Peacher J.L. 1976 *Phys. Rev.* A **14** 608–14
[14] Chong Y.P. and Fite W.L. 1977 *Phys. Rev.* A **16** 933–42
[15] Hvelplund P. and Andersen A. 1982 *Phys. Scr.* **26** 375
[16] Schartner K.H., Detleffsen D. and Sommer B. 1989 *Phys. Lett.* A **136** 55–58
[17] Kołakowska A., Pindzola M.S. and Schultz D.R. 1999 *Phys. Rev.* A **59** 3588–91
[18] Toshima N. 1999 *Phys. Rev.* A **59** 1981–7
[19] Winter T.G. 2009 *Phys. Rev.* A **80** 032701
[20] Chassid M. and Horbatsch M. 2002 *Phys. Rev.* A **66** 012714
[21] Zou S., Pichl L., Kimura M. and Kato T. 2002 *Phys. Rev.* A **66** 042707
[22] Pindzola M.S., Lee T.G., Minami T. and Schultz D.R. 2005 *Phys. Rev.* A **72** 062703
[23] Abdurakhmanov I.B., Kadyrov A.S., Avazbaev S.K. and Bray I. 2016 *J. Phys. B: At. Mol. Opt. Phys* **49** 115203
[24] Taoutioui A., Dubois A., Sisourat N. and Makhoute A. 2018 *J. Phys. B: At. Mol. Opt. Phys* **51** 235202
[25] Leung A.C.K. and Kirchner T. 2019 *Eur. Phys. J.* D **73** 246
[26] Agueny H., Hansen J.P., Dubois A., Makhoute A., Taoutioui A. and Sisourat N. 2019 *At. Data Nucl. Data Tables* **129–130** 101281
[27] Abdurakhmanov I.B., Plowman C., Kadyrov A.S., Bray I. and Mukhamedzhanov A.M. 2020 *J. Phys. B: At. Mol. Opt. Phys* **53** 145201
[28] Cariatore N.D. and Schultz D.R. 2020 *Astrophys. J. Suppl. Ser.* **252** 7
[29] Ziaeian I. and Tőkési K. 2022 *At. Data Nucl. Data Tables* **146** 101509
[30] Fritsch W. and Lin C.D. 1983 *Phys. Rev.* A **27** 3361–4
[31] Ermolaev A.M. 1990 *J. Phys. B: At. Mol. Opt. Phys* **23** L45
[32] Fainstein P.D., Ponce V.H. and Rivarola R.D. 1990 *J. Phys. B: At. Mol. Opt. Phys* **23** 1481
[33] Sidky E.Y. and Lin C.D. 2001 *Phys. Rev.* A **65** 012711
[34] von Hellermann M., de Bock M., Marchuk O., Reiter D., Serov S. and Walsh M. 2019 *Atoms* **7** 30
[35] Abdurakhmanov I.B., Kadyrov A.S. and Bray I. 2016 *Phys. Rev.* A **94** 022703
[36] Abdurakhmanov I.B., Bailey J.J., Kadyrov A.S. and Bray I. 2018 *Phys. Rev.* A **97** 032707
[37] Spicer K.H., Plowman C.T., Abdurakhmanov I.B., Kadyrov A.S., Bray I. and Alladustov S.U. 2021 *Phys. Rev.* A **104** 032818
[38] Spicer K.H., Plowman C.T., Abdurakhmanov I.B., Alladustov S.U., Bray I. and Kadyrov A.S. 2021 *Phys. Rev.* A **104** 052815
[39] Plowman C.T., Abdurakhmanov I.B., Bray I. and Kadyrov A.S. 2022 *Eur. Phys. J.* D **76** 31
[40] Plowman C.T., Abdurakhmanov I.B., Bray I. and Kadyrov A.S. 2022 *Eur. Phys. J.* D **76** 129
[41] Plowman C.T., Abdurakhmanov I.B., Bray I. and Kadyrov A.S. 2023 *Phys. Rev.* A **107** 032824
[42] Abdurakhmanov I.B., Massen-Hane K., Alladustov S.U., Bailey J.J., Kadyrov A.S. and Bray I. 2018 *Phys. Rev.* A **98** 062710
[43] Abdurakhmanov I.B., Alladustov S.U., Bailey J.J., Kadyrov A.S. and Bray I. 2018 *Plasma Phys. Control. Fusion* **60** 095009
[44] Faulkner J., Abdurakhmanov I.B., Alladustov S.U., Kadyrov A.S. and Bray I. 2019 *Plasma Phys. Control. Fusion* **61** 095005
[45] Alladustov S.U., Abdurakhmanov I.B., Kadyrov A.S., Bray I. and Bartschat K. 2019 *Phys. Rev.* A **99** 052706
[46] Abdurakhmanov I.B., Erkilic O., Kadyrov A.S., Bray I., Avazbaev S.K. and Mukhamedzhanov A.M. 2019 *J. Phys. B: At. Mol. Opt. Phys.* **52** 105701
[47] Antonio N.W., Plowman C.T., Abdurakhmanov I.B., Bray I. and Kadyrov A.S. 2021 *J. Phys. B: At. Mol. Opt. Phys.* **54** 175201
[48] Abdurakhmanov I.B., Plowman C.T., Spicer K.H., Bray I. and Kadyrov A.S. 2021 *Phys. Rev.* A **104** 042820
[49] Antonio N.W., Plowman C.T., Abdurakhmanov I.B., Bray I. and Kadyrov A.S. 2022 *Phys. Rev.* A **106** 012822
[50] Kotian A.M., Plowman C.T., Abdurakhmanov I.B., Bray I. and Kadyrov A.S. 2022 *J. Phys. B: At. Mol. Opt. Phys.* **55** 115201
[51] Antonio N.W., Plowman C.T., Abdurakhmanov I.B., Bray I. and Kadyrov A.S. 2022 *Atoms* **10** 137

[52] Kotian A.M., Plowman C.T., Abdurakhmanov I.B., Bray I. and Kadyrov A.S. 2022 *Atoms* **10** 144

[53] Alladustov S.U., Plowman C.T., Abdurakhmanov I.B., Bray I. and Kadyrov A.S. 2022 *Phys. Rev. A* **106** 062819

[54] Jorge A., Suárez J., Illescas C., Errea L.F. and Méndez L. 2016 *Phys. Rev. A* **94** 032707

[55] Jorge A., Illescas C. and Méndez L. 2022 *Phys. Rev. A* **105** 012811

[56] Suarez J., Farantos S., Stamatiadis S. and Lathouwers L. 2009 *Comput. Phys. Commun.* **180** 2025–33

[57] Bransden B.H. and McDowell M.R.C. 1992 *Charge Exchange and the Theory of Ion-Atom Collisions* (Clarendon)

[58] Fritsch W. and Lin C. 1991 *Phys. Rep.* **202** 1–97

[59] Gao J.W., Wu Y., Sisourat N., Wang J.G. and Dubois A. 2017 *Phys. Rev. A* **96** 052703

[60] Liu L., Wu Y., Wang J.G. and Janev R.K. 2022 *At. Data Nucl. Data Tables* **143** 101464

[61] Kroneisen O.J., Lüdde H.J., Kirchner T. and Dreizler R.M. 1999 *J. Phys. A: Math. Gen.* **32** 2141

[62] Zapukhlyak M., Kirchner T., Lüdde H.J., Knoop S., Morgenstern R. and Hoekstra R. 2005 *J. Phys. B: At. Mol. Opt. Phys.* **38** 2353

[63] Lüdde H.J., Horbatsch M. and Kirchner T. 2018 *Eur. Phys. J. B* **91** 99

[64] Lüdde H.J., Kalkbrenner T., Horbatsch M. and Kirchner T. 2020 *Phys. Rev. A* **101** 062709

[65] Leung A.C.K. and Kirchner T. 2021 *Atoms* **10** 11

[66] Abrines R. and Percival I.C. 1966 *Proc. Phys. Soc.* **88** 861–72

[67] Olson R.E. and Salop A. 1977 *Phys. Rev. A* **16** 531–41

[68] Schultz D.R., Meng L. and Olson R.E. 1992 *J. Phys. B: At. Mol. Opt. Phys.* **25** 4601

[69] Tőkési K. and Hock G. 1994 *Nucl. Instrum. Methods Phys. Res. B* **86** 201–4

[70] Tőkési K. and Hock G. 1996 *J. Phys. B: At. Mol. Opt. Phys.* **29** L119

[71] Bachi N. and Otranto S. 2018 *Eur. Phys. J. D* **72** 127

[72] Ziaeian I. and Tőkési K. 2021 *Eur. Phys. J. D* **75** 138

[73] Asztalos O., Szondy B., Tőkési K. and Pokol G. 2019 *Eur. Phys. J. D* **73** 116

[74] Tőkési K. and Kövér A. 1999 *Nucl. Instrum. Methods Phys. Res. B* **154** 259–62

[75] Tőkési K. and Kövér A. 2000 *J. Phys. B: At. Mol. Opt. Phys* **33** 3067

[76] Becker R.L. and MacKellar A.D. 1984 *J. Phys. B: At. Mol. Phys.* **17** 3923–42

[77] Hardie D.J.W. and Olson R.E. 1983 *J. Phys. B: At. Mol. Phys.* **16** 1983–96

[78] Illescas C., Rabadán I. and Riera A. 1998 *Phys. Rev. A* **57** 1809–20

[79] Jorge A., Errea L., Illescas C. and Méndez L. 2014 *Eur. Phys. J. D* **68** 227

[80] Errea L.F., Illescas C., Méndez L., Pons B., Riera A. and Suárez J. 2004 *Phys. Rev. A* **70** 052713

[81] Guzmán F., Errea L.F., Illescas C., Méndez L. and Pons B. 2010 *J. Phys. B: At. Mol. Opt. Phys* **43** 144007

[82] Kirschbaum C.L. and Wilets L. 1980 *Phys. Rev. A* **21** 834–41

[83] Cohen J.S. 1996 *Phys. Rev. A* **54** 573–86

[84] Ziaeian I. and Tőkési K. 2022 *J. Phys. B: At. Mol. Opt. Phys.* **55** 245201

[85] Al Atawneh S.J. and Tőkési K. 2022 *Phys. Chem. Chem. Phys.* **24** 15280–91

[86] Ziaeian I. and Tőkési K. 2020 *Atoms* **8** 27

[87] Ziaeian I. and Tőkési K. 2021 *Sci. Rep.* **11** 20164

[88] Ziaeian I. and Tőkési K. 2022 *Atoms* **10** 90

[89] Atawneh S.J.A., Asztalos O., Szondy B., Pokol G.I. and Tőkési K. 2020 *Atoms* **8** 31

[90] Atawneh S.J.A. and Tőkési K. 2021 *J. Phys. B: At. Mol. Opt. Phys.* **54** 065202

[91] Atawneh S.J.A. and Tőkési K. 2021 *Nucl. Fusion* **62** 026009

[92] Atawneh S.J.A. and Tőkési K. 2022 *At. Data Nucl. Data Tables* **146** 101513

[93] Igenbergs K., Schweinzer J. and Aumayr F. 2009 *J. Phys. B: At. Mol. Opt. Phys.* **42** 235206

[94] Janev R.K., Reiter D. and Samm U. 2003 *Collision Processes in Low-Temperature Hydrogen Plasmas* vol 4105 (Forschungszentrum Jülich)

[95] McCartney M. and Crothers D.S.F. 1995 *Z. Phys. D* **35** 1–2

[96] Olivera G.H., Rivarola R.D. and Fainstein P.D. 1995 *Phys. Rev. A* **51** 847–9

[97] Hutchinson I.H. 2001 *Plasma Phys. Control. Fusion* **44** 71

[98] O'Mullane M. 2009 Review of proton impact driven ionisation from the excited levels in neutral hydrogen beams (available at: www.adas.ac.uk/notes/adas_c09-01. pdf)

[99] Schuch R. 2019 Interference effects in electron capture collisions *Ion-Atom Collisions: The Few-Body Problem in Dynamic Systems* ed M. Schulz (De Gruyter) pp 179–211

[100] Lee J.K., Lee H.H., Ko W.H., Na B., Ko J., Lee M.W. and Lee S.G. 2022 *AIP Adv.* **12** 055111

[101] Ko W.H., Lee H.H., Jeon Y.M., Ida K., Lee J.H., Yoon S.W., Lee K.D., Bae Y.S., Oh Y.K. and Kwak J.G. 2014 *Rev. Sci. Instrum.* **85** 11E413

[102] Ko J. and Chung J. 2017 *Rev. Sci. Instrum.* **88** 063505

[103] Reimer R., Marchuk O., Geiger B., Mc Carthy P.J., Dunne M., Hobirk J. and Wolf R. 2017 *Rev. Sci. Instrum.* **88** 083509

[104] Boley C.D., Janev R.K. and Post D.E. 1984 *Phys. Rev. Lett.* **52** 534–7

[105] Janev R., Langer W., Post D. and Evans K. 1987 *Elementary Processes in Hydrogen-Helium Plasmas* (Springer)

[106] OPEN-ADAS (Atomic Database and Analysis Structures) (available at: https://open.adas.ac.uk/) (Retrieved 8 September 2023)

[107] Klyuchnikov L.A., Krupin V.A., Nurgaliev M.R., Korobov K.V., Nemets A.R., Dnestrovskij A.Y., Tugarinov S.N., Serov S.V. and Naumenko N.N. 2016 *Rev. Sci. Instrum.* **87** 053506

[108] Spence J. and Summers H.P. 1986 *J. Phys. B: At. Mol. Phys.* **19** 3749

[109] Bespamyatnov I.O., Rowan W.L. and Liao K.T. 2012 *Comput. Phys. Commun.* **183** 669

[110] Barnett C.F., Hunter H.T., Fitzpatrick M.I., Alvarez I., Cisneros C. and Phaneuf R.A. 1990 Atomic data for fusion. Volume 1: collisions of H, H_2, He and Li atoms and ions with atoms and molecules *Technical Report* (Oak Ridge National Laboratory)

[111] Fonck R.J., Darrow D.S. and Jaehnig K.P. 1984 *Phys. Rev. A* **29** 3288–309

[112] Marchuk O., Ralchenko Y., Janev R.K., Bertschinger G. and Biel W. 2009 *J. Phys. B: At. Mol. Opt. Phys.* **42** 165701

[113] Schlummer T., Marchuk O., Schultz D.R., Bertschinger G., Biel W. and Reiter D. (The TEXTOR-Team) 2015 *J. Phys. B: At. Mol. Opt. Phys.* **48** 144033

[114] McDermott R., Dux R., Guzman F., Pütterich T., Fischer R. and Kappatou A. (The ASDEX Upgrade Team) 2020 *Nucl. Fusion* **61** 016019

[115] Marchuk O., Ralchenko Y., Schultz D.R., Biel W. and Schlummer T. (TEXTOR Team) 2013 *AIP Conf. Proc.* **1545** 153–63

[116] Isler R.C. 1994 *Plasma Phys. Control. Fusion* **36** 171

[117] Marchuk O., Delabie E., Bertschinger G., Biel W., Jaspers R. and von Hellermann M. 2009 Influence of collisions on the emission of neutral beams *36th EPS Conf. on Plasma Physics* (*Sofia, Bulgaria, 29 June–3 July 2009*) vol 33E P-5.212

[118] Sampson D.H. 1977 *J. Phys. B: At. Mol. Phys.* **10** 749

[119] Bethe H. and Salpeter E. 2014 *Quantum Mechanics of One-and Two-Electron Atoms* (Springer)

[120] Damburg R.J. and Kolosov V.V. 1978 *J. Phys. B: At. Mol. Phys.* **11** 1921

[121] Marchuk O. and Ralchenko Y. 2012 *Populations of Excited Parabolic States of Hydrogen Beam in Fusion Plasmas* (Springer) pp 83–101

[122] Gu M.F., Holcomb C.T., Jayakuma R.J. and Allen S.L. 2008 *J. Phys. B: At. Mol. Opt. Phys.* **41** 095701

[123] Marchuk O., Schultz D.R. and Ralchenko Y. 2020 *Atoms* **8** 8

[124] Abdurakhmanov I.B., Kadyrov A.S. and Bray I. 2016 *J. Phys. B: At. Mol. Opt. Phys* **49** 03LT01

[125] Burke M.G., Fonck R.J., Mckee G.R. and Winz G.R. 2023 *Rev. Sci. Instrum.* **94** 033504

[126] Marchuk O., Ralchenko Y., Janev R., Delabie E., Biel W. and Urnov A. 2010 *Nucl. Instrum. Methods Phys. Res.* A **623** 738–40

[127] Guszejnov D., Pokol G.I., Pusztai I., Refy D., Zoletnik S., Lampert M. and Nam Y.U. 2012 *Rev. Sci. Instrum.* **83** 113501

[128] Asztalos O., Andorfi I., Balazs P., Szondy B. and Pokol G. 2022 *RENATE-OD, GitHub Repository* (available at: https://github.com/gergopokol/renate-od)

[129] Asunta O., Govenius J., Budny R., Gorelenkova M., Tardini G., Kurki-Suonio T., Salmi A. and Sipilä S. 2015 *Comput. Phys. Commun.* **188** 33–46

[130] Geiger B. *et al* 2020 *Plasma Phys. Control. Fusion* **62** 105008

[131] Carr M., Meakins A., Bernert M., David P., Giroud C., Harrison J., Henderson S., Lipschultz B. and Reimold F. (EUROfusion MST1 Team and ASDEX Upgrade Team) 2018 *Rev. Sci. Instrum.* **89** 083506

[132] Pokol G.I. *et al* 2021 Neutral beam penetration and photoemission benchmark *47th EPS Conf. on Plasma Physics* (*Sitges, Spain*, *21–25 June*) 45A, P1.1007

[133] Pokol G.I. *et al* 2022 Outcome of the IAEA neutral beam penetration and photoemission benchmark *32nd Symp. on Fusion Technology* (*Dubrovnik, Croatia*, *18–23 September*) P-2.298

[134] Johnson L. 1972 *Astrophys. J.* **174** 227–36

[135] Schweinzer J., Wolfrum E., Aumayr F., Pockl M., Winter H., Schorn R.P., Hintz E. and Unterreiter A. 1992 *Plasma Phys. Control. Fusion* **34** 1173–83

[136] Hill C., Dipti, Asztalos O., Pokol G. and Haničinec M. 2022 CollisionDB: a new database of atomic and molecular collisional processes with an interactive API (private communication)

[137] Murakami I., Kato M., Emoto M., Kato D., Sakaue H.A. and Kawate T. 2020 *Atoms* **8** 71

[138] Pitchford L.C. *et al* 2017 *Plasma Process. Polym.* **14** 1600098

[139] Kwon D.H. and Chai K.B. (KAERI Atomic Data Center Team) *Photonic Electronic Atomic Reaction Laboratory Database* (available at: http://pearl.kaeri.re.kr/pearl/)

[140] Hulse R.A. 1990 *AIP Conf. Proc.* **206** 63–72

[141] Hill C. 2022 *PyValem, GitHub Repository* (available at: https://github.com/xnx/pyvalem)

[142] Hill C. *et al* 2022 Classification of processes in plasma physics, version 2.4 (available at: https://amdis.iaea.org/media/miscellaneous-publications/plasma-processes-classification-v2.4.pdf)

[143] Skinner F., Gordon I., Hill C., Hargreaves R., Lockhart K. and Rothman L. 2020 *Atoms* **8** 16

[144] Hill C. 2022 *django-pyref, GitHub Repository* (available at: https://github.com/xnx/django-pyref)

[145] Atomic and plasma–material interaction data for fusion 1991–Present (IAEA Journal Series)

[146] Hill C. 2022 *PyCollisionDB, GitHub Repository* (available at: https://github.com/xnx/pycollisiondb)

[147] Avazbaev S.K., Kadyrov A.S., Abdurakhmanov I.B., Fursa D.V. and Bray I. 2016 *Phys. Rev.* A **93** 022710

[148] Zeng S.L., Liu L., Wang J.G. and Janev R.K. 2008 *J. Phys. B: At. Mol. Opt. Phys.* **41** 135202

[149] Liu L., Wang J.G. and Janev R.K. 2008 *Phys. Rev.* A **77** 032709

[150] Liu L., Wang J.G. and Janev R.K. 2008 *Phys. Rev.* A **77** 042712

[151] Liu C.L., Zou S.Y., He B. and Wang J.G. 2015 *Chin. Phys.* B **24** 093402

[152] Ibaaz A., Hernandez R.E., Dubois A. and Sisourat N. 2016 *J. Phys. B: At. Mol. Opt. Phys* **49** 085202

[153] Wu Y., Liu L., Liu C.H., Qu Y.Z., Wang J.G. and Janev R.K. 2015 *J. Phys.: Conf. Ser.* **576** 012012

[154] Jakimovski D., Liu L., Wang J.G. and Janev R.K. 2010 *J. Phys. B: At. Mol. Opt. Phys.* **43** 165202

[155] Caillat J., Dubois A. and Hansen J.P. 2000 *J. Phys. B: At. Mol. Opt. Phys* **33** L715

[156] Hansen J.P. and Dubois A. 1998 *J. Phys. B: At. Mol. Opt. Phys* **31** L861

[157] Wang J., Hansen J.P. and Dubois A. 2000 *J. Phys. B: At. Mol. Opt. Phys* **33** 241

[158] Wang J.B., Hansen J.P. and Dubois A. 2000 *Phys. Rev. Lett.* **85** 1638–41

[159] Bailey J.J., Abdurakhmanov I.B., Kadyrov A.S., Bray I. and Mukhamedzhanov A.M. 2019 *Phys. Rev.* A **99** 042701

[160] Jorge A., Illescas C., Méndez L. and Pons B. 2016 *Phys. Rev.* A **94** 022710

[161] Liu C.H., Wang J.G. and Janev R.K. 2012 *J. Phys. B: At. Mol. Opt. Phys.* **45** 235203

[162] Guo D.L. *et al* 2021 *Phys. Rev.* A **103** 032827

[163] Liu C.H., Wang J.G. and Janev R.K. 2012 *Phys. Rev.* A **85** 042719

[164] Liu L., Jakimovski D., Wang J.G. and Janev R.K. 2012 *J. Phys. B: At. Mol. Opt. Phys.* **45** 225203

[165] Dubois A. and Hansen J.P. 2001 *Eur. Phys. J.* D **13** 207

[166] Ma M.X., Kou B.H., Liu L., Wu Y. and Wang J.G. 2020 *Chin. Phys.* B **29** 013401

[167] Dubois A., Nielsen S.E. and Hansen J.P. 1993 *J. Phys. B: At. Mol. Opt. Phys* **26** 705